

High-Resolution Mid-Infrared Spectroscopy of GV Tau N: Surface Accretion and Detection of NH_3 in a Young Protoplanetary Disk

Joan R. Najita

NSF's NOIRLab, 950 N. Cherry Avenue, Tucson, AZ 85719, USA

John S. Carr

Department of Astronomy, University of Maryland, College Park, MD 20742, USA

Sean D. Brittain

Clemson University, 118 Kinard Laboratory, Clemson, SC 29634, USA

John H. Lacy

Department of Astronomy, University of Texas at Austin, Austin, TX 78712, USA

Matthew J. Richter

Physics Department, University of California at Davis, Davis, CA 95616, USA

Greg W. Doppmann

W. M. Keck Observatory, 65-1120 Mamalahoa Hwy., Kamuela, HI 96743, USA

ABSTRACT

Physical processes that redistribute or remove angular momentum from protoplanetary disks can drive mass accretion onto the star and affect the outcome of planet formation. Despite ubiquitous evidence that protoplanetary disks are engaged in accretion, the process(es) responsible remain unclear. Here we present evidence for redshifted molecular absorption in the spectrum of a Class I source that indicates rapid inflow at the disk surface. High resolution mid-infrared spectroscopy of GV Tau N reveals a rich absorption spectrum of individual lines of C_2H_2 , HCN , NH_3 , and H_2O . From the properties of the molecular absorption, we can infer that it carries a significant accretion rate $\dot{M}_{\text{abs}} \sim 10^{-8} - 10^{-7} M_{\odot} \text{ yr}^{-1}$, comparable to the stellar accretion rates of active T Tauri stars. Thus we may be observing disk accretion in action. The results may provide observational evidence for supersonic “surface accretion flows,” which have been found in MHD simulations of magnetized disks. The observed spectra also represent the first detection of NH_3 in the planet formation region of a protoplanetary disk. With NH_3 only comparable in abundance to HCN , it cannot be a major missing reservoir of nitrogen. If, as expected, the dominant nitrogen reservoir in inner disks is instead N_2 , its high volatility would make it difficult to incorporate into forming planets, which may help to explain the low nitrogen content of the bulk Earth.

Subject headings: T Tauri stars, protoplanetary disks, stellar accretion disks, circumstellar disks, planet formation, interstellar molecules

1. Introduction

Stars form surrounded by disks, the repositories of excess angular momentum inherited from the molecular cloud that cannot be contained within the star alone. Physical processes that redistribute or remove disk angular momentum can drive mass accretion onto the star and affect the outcome of planet formation; e.g., giant planets that form in the disk may be swept inward along with the accretion flow. Although it is as yet unclear what physical mechanism(s) generate accretion flows, the process(es) must be robust: T Tauri stars (i.e., young stars surrounded by disks) commonly show excess UV emission produced by mass flows that reach the stellar surface (Hartmann et al. 2016).

One clue to the nature of disk accretion comes from the sizes of gaseous disks. Whereas disks in the embedded “Class I” phase of pre-main-sequence evolution are modest in size (typically < 100 au in radius), gas disks in the more evolved “Class II” phase, when infall from the molecular cloud has ceased, span a range of sizes including many much larger than 300 au (Najita & Bergin 2018; Ansdell et al. 2018). The existence of such large disks is remarkable given the multiple processes that can act to reduce disk sizes (e.g., FUV photoevaporation, companion formation, disk winds). Their existence suggests that internal angular momentum redistribution plays a large enough role in driving accretion that a significant fraction of disks grow substantially in size from the Class I to Class II phases (Najita & Bergin 2018). However there have been few observational clues to date as to the nature of the process that redistributes the angular momentum. Disk spectral line diagnostics offer the opportunity to probe the dynamics of disks for potential new insights.

Spectral features in the mid-infrared (MIR) offer the opportunity to study the dynamics and chemistry of planet formation environments. Class II (T Tauri) disks commonly reveal a MIR spectrum that is rich in emission from water and organic molecules (CO_2 , HCN, C_2H_2 ; Carr & Najita 2008, 2011; Salyk et al. 2011). The emitting areas, line profiles, and thermal-chemical properties of the emitting gas are consistent with emission from an irradiated disk atmosphere within a few au of the star, i.e., the terrestrial planet region of the disk (e.g., Najita & Ádámkóvics 2017; Najita et al. 2018). In contrast to the frequent detection of MIR molecular emission, MIR molecular *absorption* is detected only rarely from young stars at low spectral resolution. Observations with the *Spitzer Space Telescope* detected molecular absorption features of HCN, C_2H_2 , and CO_2 from IRS 46 (Lahuis et al. 2006) and GV Tau (e.g., Bast et al. 2013), and CO_2 from DG Tau B (Kruger et al. 2011; Pontoppidan et al. 2008). The similar molecular species and gas temperatures detected in emission and absorption suggested that the absorption features also arise in a disk atmosphere but viewed close to edge on (Bast et al. 2013; Doppmann et al. 2008).

Here we report high resolution MIR spectroscopy of the Class I source GV Tau N, which reveals

a rich molecular absorption spectrum of individual lines of C_2H_2 and HCN , as well as H_2O and the first detection of NH_3 in the planet formation region of a protoplanetary disk. The resolved line profiles, which have a significant redshifted component, may provide observational evidence for a new accretion mechanism: supersonic “surface accretion flows,” which have been found in MHD simulations of magnetized disks (Zhu & Stone 2018; see also Stone & Norman 1994; Beckwith et al. 2009; Guilet & Ogilvie 2012, 2013).

A young stellar binary in the Taurus molecular cloud ($d=140$ pc), GV Tau (a.k.a. Haro 6–10, IRAS 04263+2426) comprises a bright optical source, GV Tau S, and an infrared companion located $1.2''$ away, GV Tau N, which dominates the MIR flux of the system (e.g., Leinert & Haas 1989; Sheehan & Eisner 2014). While GV Tau has the strongly rising 2–25 μm continuum characteristic of Class I sources (e.g., Furlan et al. 2008), its relatively weak gas and dust emission compared to other low-mass embedded YSOs suggests that the system lacks a significant envelope (Hogerheijde et al. 1998). That property and the poorly defined molecular outflow structure of the system (Hogerheijde et al. 1998) suggest that it is a more evolved Class I source. Spatially resolved millimeter imaging further suggests modest solid disk masses for both GV Tau N and S (Sheehan & Eisner 2014) and small dust disk sizes (~ 15 au; Guilloteau et al. 2011).

In addition to the molecular absorption bands of HCN , C_2H_2 , and CO_2 detected with *Spitzer* (Bast et al. 2013), the spectrum of GV Tau N also shows individual near-infrared (NIR) absorption lines of HCN , C_2H_2 , CH_4 , and CO (Gibb et al. 2007; Doppmann et al. 2008; Gibb & Horne 2013; Davis et al. 2015). While CO absorption has been detected toward both Class I and Class II sources at high spectral resolution (Brittain et al. 2005; Rettig et al. 2006; Horne et al. 2012; Kruger et al. 2011; Smith et al. 2015; Lee et al. 2016), organic absorption features are rarely seen. Here we report a high spectral resolution observation of the MIR spectrum of GV Tau N. The observations are described in Section 2, and the detected features are analyzed in Section 3. In Section 4, we discuss the origin of the absorption features and the possible support they provide for the existence of surface accretion flows. We also comment on the detection of NH_3 and its implications for our understanding of the nitrogen reservoir in disks.

2. TEXES Observations

We observed GV Tau N with TEXES, the Texas Echelon-cross-Echelle spectrograph (Lacy et al. 2002), on the Gemini-North 8m telescope during observing campaigns in November 2006 and October 2007. We used the high resolution, cross-dispersed mode for all observations with a slit width of $0.54''$. The spectral resolving power in this instrumental configuration is $R \approx 100,000$. We nodded the object on the slit every ~ 10 seconds to facilitate background subtraction and removal of night-sky emission. TEXES does not use the chopping secondary mirror. During the first visit to GV Tau on (UT) 19 November 2006, we observed both GV Tau S and GV Tau N to confirm that the mid-IR flux originated almost entirely with GV Tau N. Subsequent to that observation, we concentrated solely on GV Tau N.

The spectral coverage in a single setting with TEXES is roughly 0.5% of the central wavenumber. Therefore, we targeted specific molecular transitions in each setting based on the telluric atmosphere, the source Doppler shift, and a desire to cover a range of lower state levels and molecules. We used the night-sky emission features to evaluate and adjust the spectral setting to avoid desired features falling into gaps in the coverage; for $\lambda \geq 11 \mu m$, the TEXES spectral orders are larger than the detector.

The standard observation sequence with TEXES includes observing an ambient temperature blackbody roughly every 7 minutes as a flatfield. We also observed a telluric calibrator, either a hot star or a featureless continuum source, immediately before or after GV Tau N. The telluric calibrator helps to reduce the impact of atmospheric absorption and to flatten the continuum beyond what division by the blackbody alone provides. A log of the observations, including the telluric calibrator used, is given in Table 1.

The data were reduced using the standard TEXES pipeline. The pipeline removes spikes, rectifies the cross-dispersed echellograms, flatfields the data, aligns and combines nod pairs, optimally extracts the spectrum of the continuum object, and does a wavelength calibration using a night-sky emission line. We subsequently divided the GV Tau N spectra by a scaled version of the telluric calibrator spectrum to remove residual atmospheric lines.

The wavelength scale was refined using telluric absorption lines in the spectrum of GV Tau N. For each setting, a dispersion function was fit to all measureable telluric lines in each order, using the IRAF task `ecidentify`.¹ The fits had an average rms residual of 0.15 km s^{-1} and an average maximum residual of 0.3 km s^{-1} . Two observations have larger uncertainties. The signal-to-noise for the 814 cm^{-1} setting from 2007 was too low to use telluric lines in the GV Tau N spectrum. Instead, the dispersion function was fit to lines in the telluric standard (rms 0.06 km s^{-1}), and this solution was applied to GV Tau N. Three measurable telluric lines in the GV Tau N spectrum were used to assign a zero-point (wavelength shift) uncertainty of 0.5 km s^{-1} . The 932 cm^{-1} setting from 2007 only contains three telluric lines; hence an independent dispersion solution was not possible. In this case, the pipeline wavelength scale was retained, with an assumed uncertainty of 1 km s^{-1} .

Model telluric transmission spectra were utilized for a few of the settings. Because the S/N for the 780 cm^{-1} setting was degraded due to insufficient S/N in the telluric calibrator, corrections for atmospheric lines were made using the software package TERRASPEC (Bender 2010). TERRASPEC was also used to improve the correction for telluric water lines in the 767 and 807 cm^{-1} settings. For all of the observations, additional continuum normalization was carried out for each order of interest by fitting a low-order polynomial to the continuum outside the intervals of absorption from known molecular transitions in GV Tau N.

¹IRAF was distributed by the National Optical Astronomy Observatory, which was managed by the Association of Universities for Research in Astronomy (AURA) under a cooperative agreement with the National Science Foundation.

3. Analysis

In the TEXES spectra we detect numerous absorption lines of NH_3 , HCN , and C_2H_2 , a few lines of H_2O in absorption, and H_2 in emission (Table 2). The H_2 emission from GV Tau was previously reported in Bitner et al. (2008) and is not discussed further here. Most of the HCN and C_2H_2 lines were measured in 2006, with additional lines measured in 2007. The unexpected detection in 2006 of numerous NH_3 absorption lines was followed up in 2007 with grating settings that probed lower energy NH_3 transitions. Weak absorption lines of water were also detected in the 2007 spectra. The entire set of pipeline-reduced spectra for GV Tau N are shown in Figure A1. The positions and identifications of the detected lines are indicated.

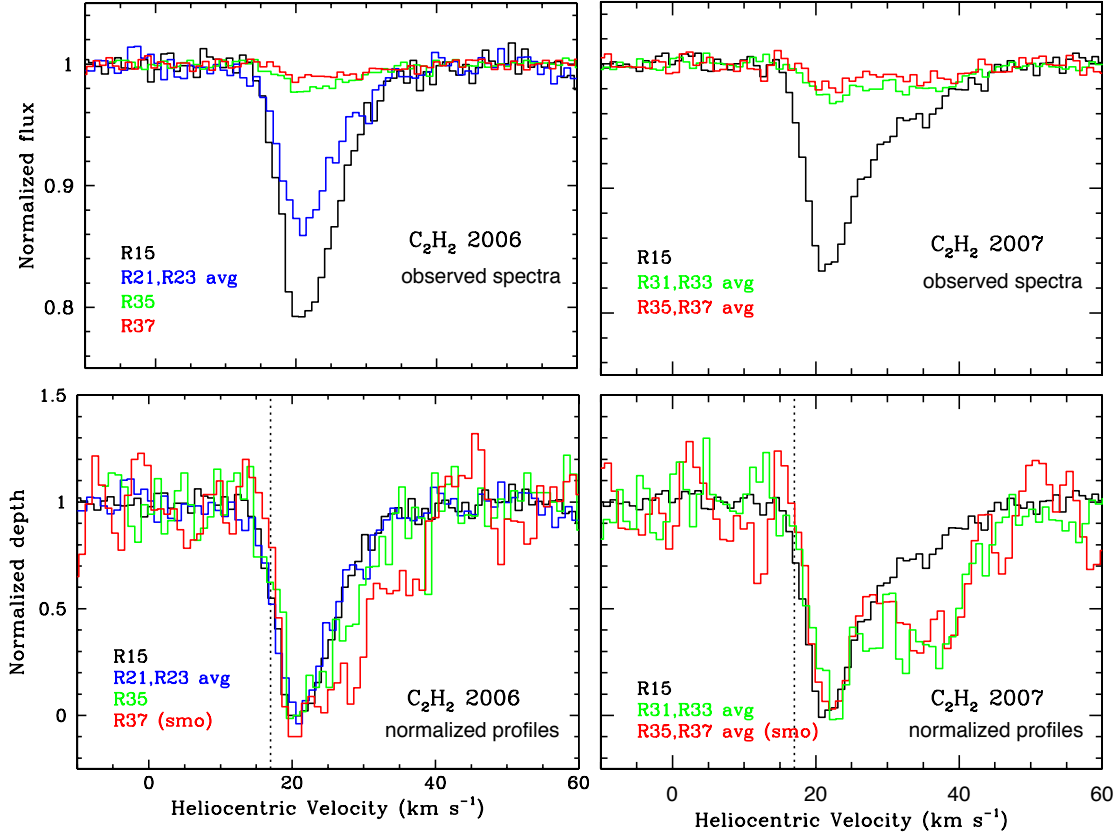


Fig. 1.— C_2H_2 spectra (top) and normalized line profiles (bottom) in 2006 (left) and 2007 (right). For reference, in the bottom panels, the vertical lines mark the velocity of the molecular cloud core from Hogerheijde et al. (1998). In the bottom panels, the profiles are scaled to extend from 0 at the bottom of the absorption to 1 in the continuum. The lines have an absorption core at $v_{\text{helio}} \simeq 20 \text{ km s}^{-1}$ and a red wing extending to $\sim 40 \text{ km s}^{-1}$. In both epochs, the strength of the red wing relative to the core is greater in the higher energy lines (above R23) than the lower energy lines.

While the H_2O lines are pure rotational transitions within the ground vibrational state, the NH_3 , HCN , and C_2H_2 absorption lines are predominantly ro-vibrational transitions out of the ground vibrational state to a higher vibrational state; the C_2H_2 $\nu_4 + \nu_5 - \nu_4$ line is an exception (see section 3.1).

The HCN ν_2 vibrational mode is the bending mode. The ν_5 mode of C_2H_2 (HCCH) is the symmetric bending mode, in which the two H atoms vibrate together, and the ν_4 mode is the antisymmetric bending mode. In the R5 transition, for example, the rotational transition is $J=5$ to $J=6$, Q5 is $J=5$ to $J=5$, and P5 is $J=5$ to $J=4$. For C_2H_2 , the H atom spin statistics cause the odd- J (ortho) lines to be three times as strong as the even- J lines, and Q-branch lines are approximately twice as strong as P- and R-branch lines. Since HCN and C_2H_2 are linear molecules in their ground vibrational states, only the quantum number J is required to label their rotational states, although the excited bending modes are split into e and f states depending on the relative orientation of the rotational axis and the bending motion.

For NH_3 , the ν_2 vibrational mode is the ‘umbrella’ mode in which the three H atoms vibrate together. The ground and ν_2 states are split by inversion splitting, with lines from the symmetric and anti-symmetric states labelled s and a. For this symmetric top molecule the rotational state is described by two quantum numbers, J (the total angular momentum) and K (the angular momentum about the symmetry axis). Line strengths depend on both J and K , but typically states with $K=3n$ are twice as strong as those with $K=3n\pm1$. J can change in a radiative transition, but K does not. Transitions are labelled by the lower state J and K .

3.1. HCN and C_2H_2

We detect a total of 8 lines of the HCN ν_2 band, 14 lines of the C_2H_2 ν_5 band, and one line from the C_2H_2 $\nu_4+\nu_5 - \nu_4$ band (i.e., absorption out of the ν_4 vibrational level; Figure A1). In 2006, we detected 12 C_2H_2 lines between R5 and R37 and 6 HCN lines between R10 and R34. In 2007, we detected 6 C_2H_2 lines between R15 and R37, as well as three HCN transitions (R17, R18, R32) with limits on two additional HCN transitions (R33 and R34). The lower energy levels of the observed lines range from $E_\ell < 100$ K to ~ 1600 K.

The absorption features range in strength from $\sim 1\%$ deep at high excitation down to a maximum of $\sim 20\%$ deep at intermediate- J values (Fig. 1 and Fig. 2). Figure 1 shows representative line profiles of C_2H_2 over a range of excitation for 2006 (left) and 2007 (right), both as observed (top) and with the absorption features scaled to the same depth (bottom) in order to compare relative velocity profiles. In the bottom panels, vertical lines indicate the velocity of the gaseous envelope surrounding GV Tau (dashed line; $v_{\text{helio}} = 17.3 \pm 0.5 \text{ km s}^{-1}$; or $v_{\text{LSR}} = 7.0 \text{ km s}^{-1}$; Hogerheijde et al. 1998). The MIR molecular absorption is clearly redshifted with respect to the molecular cloud velocity.

Figure 2 shows the HCN spectra and normalized profiles from the 2006 data; the HCN profiles from 2007 are similar. Figure 3 compares the C_2H_2 and HCN profiles for low (top) and high (bottom) excitation lines. The C_2H_2 and HCN lines have nearly identical velocity profiles.

At low- J , the HCN and C_2H_2 lines profiles both have a “single dip” core absorption component centered at $21\text{--}22 \text{ km s}^{-1}$ with a FWHM of $\sim 8\text{--}10 \text{ km s}^{-1}$, and a red wing extending to $\sim 40 \text{ km s}^{-1}$

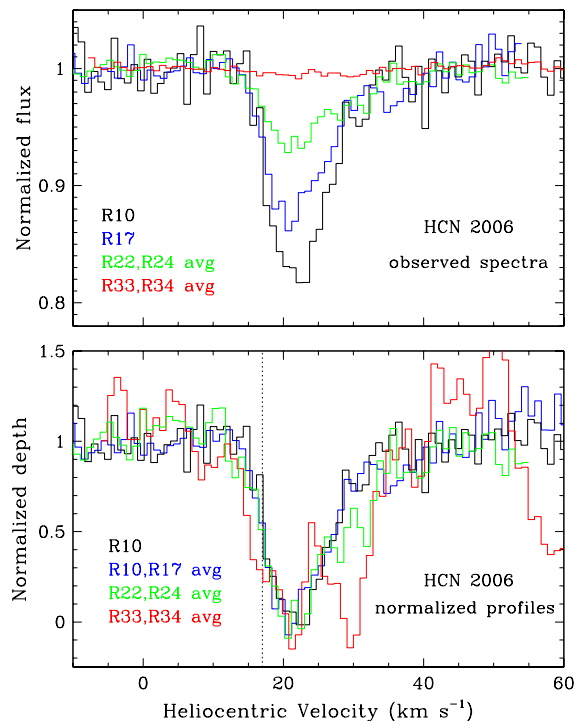


Fig. 2.— HCN spectra (top) and normalized line profiles (bottom) in 2006. Like the C_2H_2 lines, higher energy HCN lines show a red wing that is stronger relative to the core than lower energy HCN lines.

(Figs. 1, 2, 3). When scaled to the same depth, the C_2H_2 and HCN profiles show a trend in which the red wing becomes stronger (relative to the core) at high J (Fig. 1 and Fig. 2), i.e., the high velocity gas is more highly excited or is more optically thick. While low and intermediate rotational levels (e.g., R15 of C_2H_2) tend to show a wing that smoothly decreases in strength to the red, higher excitation lines show more velocity structure. For example, the C_2H_2 R37 line could be fit with velocity components at 21, 28, and 36 km s^{-1} . The velocity structure of the NH_3 (§3.2) and H_2O (§3.3) lines is similar to that seen in the HCN and C_2H_2 lines, suggesting that the molecular absorption is composed of multiple velocity components.

If the absorbing gas is optically thin, the odd- J C_2H_2 lines should be approximately 3 times stronger than the adjacent even- J lines. For several of the stronger C_2H_2 lines observed (R14 vs. R15; R21 vs. the average of R20 and R22; R23 vs. the average of R22 and R24), the ratio of the absorption depths of the ortho and para lines is lower, ~ 2 in the absorption core (Fig. 4), indicating that the odd- J lines have optical depths of ~ 1 or greater. The relative depths of the neighboring ortho-para lines also differ between the core and the wing. The ratio of the absorption depths declines from ~ 2 within the absorption core to ~ 1 in the red wing beyond 30 km s^{-1} (Fig. 4), indicating that the even- J C_2H_2 lines are also optically thick in the high velocity gas. Interestingly, the observed depths of the C_2H_2 lines ($< 20\%$) are far less than expected for optically thick lines. This suggests that the line strengths are significantly diluted, or an intrinsically narrow

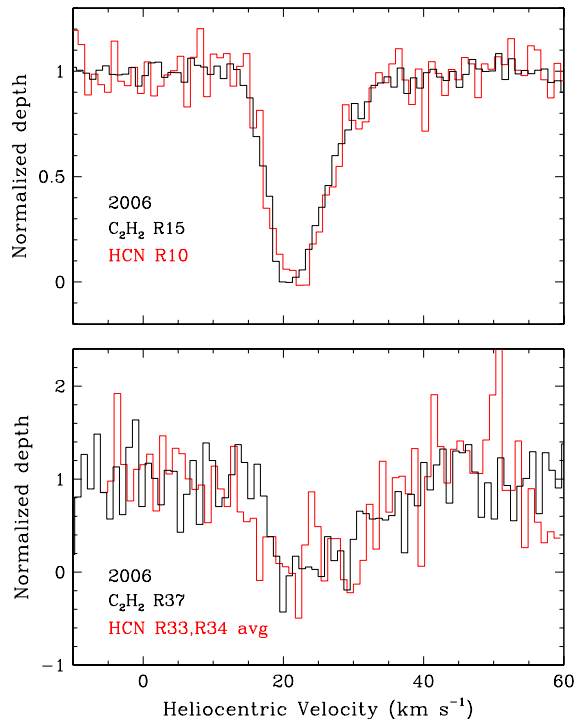


Fig. 3.— The HCN and C_2H_2 lines showed similar profiles at low- J (top) and high- J (bottom) in 2006 and 2007 (not shown), suggesting that the HCN and C_2H_2 absorption arise in the same gas along the line of sight.

line is highly broadened by macroscopic motions, or some combination of these two effects.

3.2. NH_3

We detect a total of 34 lines of the NH_3 ν_2 band (Figure A1): 12 transitions in 2006 with lower energy levels from 358 cm^{-1} to 888 cm^{-1} , and 27 transitions in 2007 with lower energy levels from 17 cm^{-1} to 1581 cm^{-1} . The NH_3 absorption strengths are similar to those of the C_2H_2 and HCN lines and range in strength from $\sim 1\%$ deep for the weakest measured lines to a maximum of $\sim 30\%$ deep for the aQ(3,3) transition measured in 2007. Example spectra for individual NH_3 lines are shown in Figure 5 for several P-branch lines from 2006 and Q-branch lines from 2007.

The profiles of the NH_3 P-branch lines are roughly similar to the C_2H_2 and HCN profiles, although there are differences in detail. Figure 6 compares the C_2H_2 R15 line ($E_\ell = 282\text{ cm}^{-1}$) with the average of four aP(6,K) NH_3 lines from 2006 ($E_\ell = 384 - 417\text{ cm}^{-1}$). Like the HCN and C_2H_2 line profiles discussed in the previous section, the P-branch NH_3 line profiles also have an absorption core at $\sim 22\text{ km s}^{-1}$ and a red wing extending to $\sim 40\text{ km s}^{-1}$. However, the shape of the NH_3 core is more square bottomed, with a small shift in the velocity of the blue edge. In addition, the aP(6,K) NH_3 lines from 2006 show weak emission blueward of the absorption. A

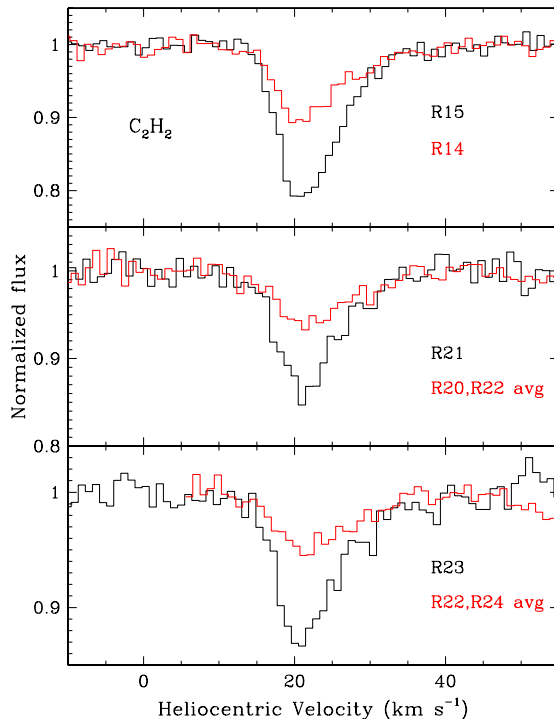


Fig. 4.— Comparison of C_2H_2 ortho and para lines in 2006. If the absorbing gas is optically thin, the odd- J lines should be approximately 3 times stronger than the adjacent even- J lines. The more modest ratio of the absorption depths implies that the absorbing gas is marginally optically thick. The relative absorption depths approach unity in the red wing, indicating larger optical depths than in the line core.

similar emission component is not seen in the line profiles of the other molecules, nor in the profiles of other NH_3 lines (including the aP(6,K) lines from 2007); however, the latter could be due to lower signal-to-noise of the other spectra. Similar line profiles are predicted in radiative transfer models of disk atmospheres with modest radial flows (see Section 4.2).

Similar to C_2H_2 and HCN, the higher velocity red wing of the NH_3 profiles becomes stronger, relative to the core, for higher excitation lines. Figure 7 compares the average 2007 profile of the aP(6,K) lines ($E_\ell = 384 - 417 \text{ cm}^{-1}$) with that of the sP(8,3) line ($E_\ell = 679 \text{ cm}^{-1}$). The higher energy line clearly shows enhanced absorption at higher velocities in the red wing.

Perhaps surprisingly, the Q-branch lines show the $\sim 22 \text{ km s}^{-1}$ core absorption component (FWHM $\sim 8 \text{ km s}^{-1}$) but *lack* the red wing. Figure 8 compares the average 2007 line profiles of the Q-branch ($E_\ell = 17 - 423 \text{ cm}^{-1}$) and aP(6,K) lines. The profile shapes differ markedly, with the higher velocity absorption in the red wing absent in the Q-branch lines. The average Q-branch profile is sharper and centered more to the red than the flat-bottomed P-branch lines. However, the Q-branch profiles also vary with line strength (see Fig. 5, bottom), with the weaker Q-branch lines closer in shape and velocity to those of the aP(6,K) lines. The absence of the red wing in the Q-branch lines may have something to do with the fact that the Q-branch transitions overlap the

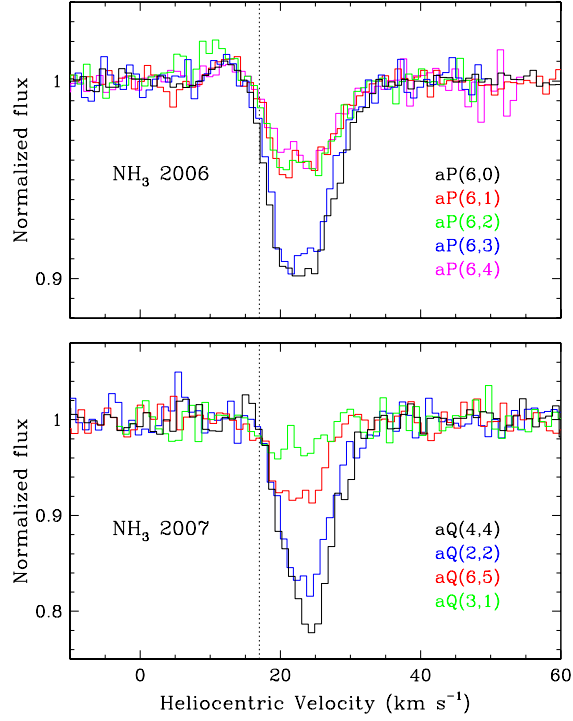


Fig. 5.— Spectra of NH₃ absorption lines. The top panel shows the aP(6,K) transitions observed in 2006. The two strongest lines have twice the statistical weight of the others but similar profiles. The bottom panel shows a selection of Q-branch lines of various strengths observed in 2007. The weaker lines have a more flat-bottomed profile and a bluer velocity centroid.

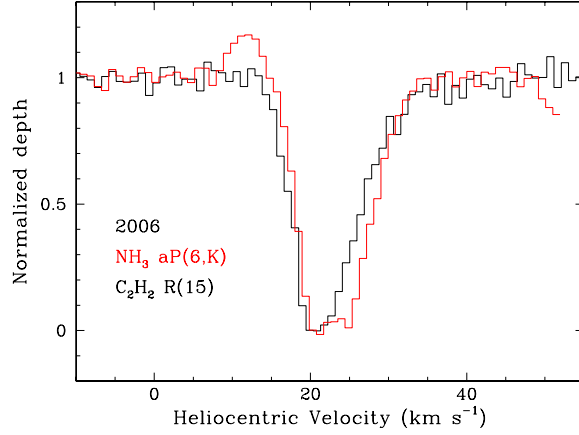


Fig. 6.— Comparison of the 2006 NH₃ aP(6,K) average profile with that of the C₂H₂ R15 reveals similar profiles, suggesting that the NH₃ and C₂H₂ arise in the gas along similar lines of sight.

10 μ m silicate absorption feature, while the measured P-branch lines fall between 12 and 13 μ m. Detailed radiative transfer models that include these opacity differences may be able to help us understand the origin of the differences in the profiles.

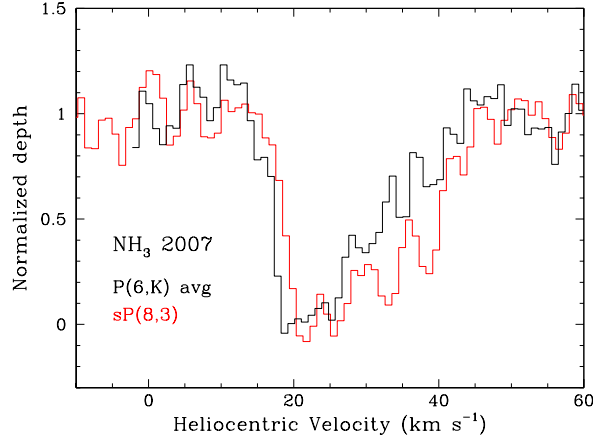


Fig. 7.— Comparison of the NH_3 aP(6,K) average profile ($E_\ell \sim 400 \text{ cm}^{-1}$) and the sP(8,3) profile ($E_\ell = 679 \text{ cm}^{-1}$) observed in 2007 shows that, like the C_2H_2 and HCN lines, the high velocity wing is stronger in the higher energy transitions.

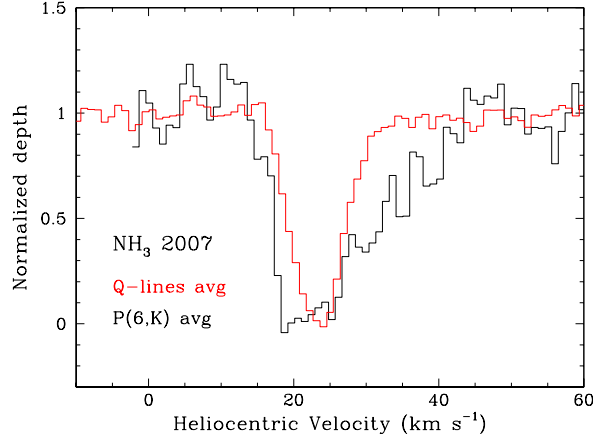


Fig. 8.— Comparison of NH_3 profiles for an average of seven Q-branch lines and four aP(6,K) lines of similar energy in 2007. The line shapes differ markedly, with the Q-branch NH_3 lines lacking much of a red wing.

3.3. H_2O

We detected 4 high excitation lines of H_2O in the 2007 spectra (Figure A1), with lower energy levels ranging from 2631 cm^{-1} to 3211 cm^{-1} . All of the lines are very weak, $\sim 2\text{--}3\%$ deep. In contrast to the C_2H_2 , HCN, and NH_3 lines, which have a prominent absorption core at $\sim 22 \text{ km s}^{-1}$, the H_2O absorption is deepest at $\sim 37 \text{ km s}^{-1}$.

Figure 9 compares the average spectrum and profile of the four detected H_2O lines with spectra and profiles of high-excitation (average of R31 and R33) and low-excitation (R15) lines of C_2H_2 in the 2007 data. The comparison shows that the H_2O absorption profile is strongest in the far red wing of the low- J C_2H_2 absorption profile. The H_2O absorption is very weak in the region of the 22 km s^{-1} component and intermediate in strength at $\sim 28 \text{ km s}^{-1}$. The profile of the higher energy C_2H_2 line, whose overall strength is weak, like the H_2O absorption, is intermediate between

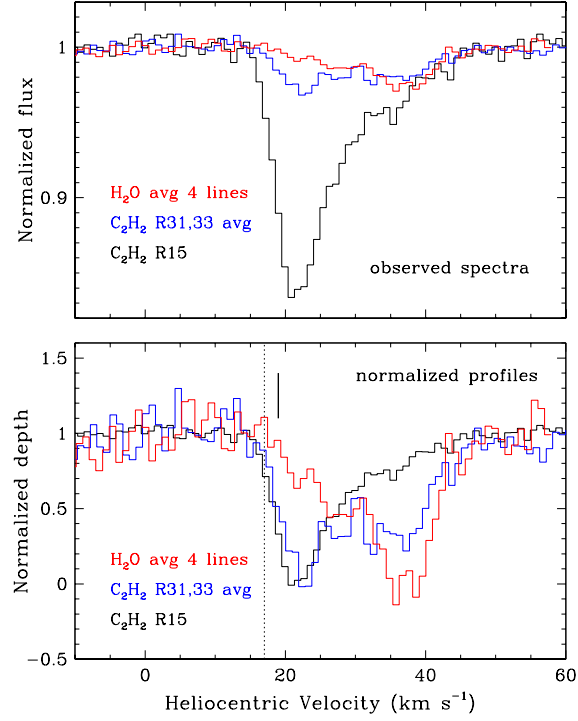


Fig. 9.— Comparison of spectra (top) and normalized line profiles (bottom) of water lines in 2007 to C₂H₂ lines. The short solid vertical line marks the position of the telluric water absorption. The vertical dotted line marks the velocity of the molecular cloud core.

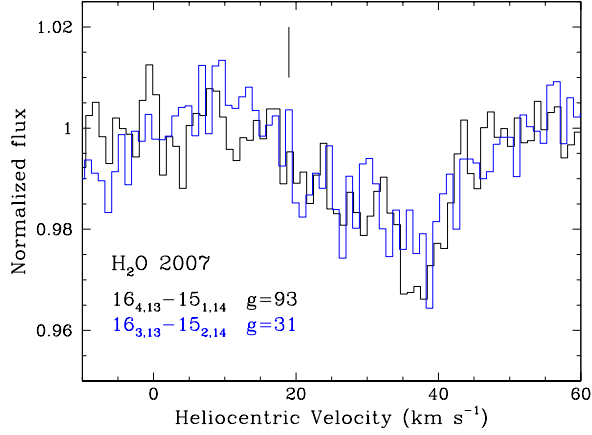


Fig. 10.— The similar strengths of ortho and para water lines in 2007 reveals that the absorption is optically thick. The short solid vertical line marks the position of the telluric water absorption.

the two profiles: it has the same velocity components as H₂O (at roughly 22 km s⁻¹, 28 km s⁻¹, and 36 km s⁻¹) but with more equal depths.

Figure 10 compares the profiles of the 16_{3,13}-15_{2,14} and 16_{4,13}-15_{1,14} water lines, which are an

ortho-para pair; they have nearly identical Einstein A-values and lower level energies (Table 2) but differ by a factor of 3 in their statistical weights. The absorption strengths of the two transitions are essentially the same, which shows that the absorption is optically thick. At the same time, the absorption depths are very small, which implies that the absorption is highly diluted, either because the absorber covers a small fraction (filling factor) of the background continuum and/or an intrinsically narrow, deeper absorption feature is broadened by macroscopic motions. A similar, but less extreme, result was found for the C_2H_2 absorption.

Table 2 lists 4 the detected water lines as well as an additional 4 undetected water lines that were used to constrain the properties of the water absorption.

3.4. Variability

There are some differences in the absorption strength and velocity profiles of the lines observed in 2006 and 2007. Figure 11 compares the 2006 and 2007 spectra of C_2H_2 for the R15 line and the average of two high excitation lines. In 2007 the core of the R15 line decreased in strength, while the red wing has increased. In the high excitation lines, the wing also increased in strength in 2007 while the 22 km s^{-1} core remained about the same. The same behavior is seen for HCN. The increase in the depth of the red wing relative to the core is common to all transitions and to all three molecules, including the P-branch NH_3 lines observed in both epochs.

A more subtle change is a small redward shift in the blue edge of the lower excitation C_2H_2 and HCN lines, resulting in a change of the line centroid from 22 to 23 km s^{-1} . These velocities differ from the average velocity of 19 km s^{-1} that Doppmann et al. (2008) found for the $3 \mu\text{m}$ HCN lines, in spectra with 13 km s^{-1} resolution that did not resolve the line profiles. Hence, velocity variations may be common, but the TEXES data show that this can be produced by changes in the velocity structure of the absorption, rather than just a simple velocity shift of the entire profile.

3.5. Equivalent Widths and Absorption Properties

The equivalent widths (EWs) of the absorption features were used to infer the temperatures and column densities of the absorbing molecules. Because there are differences in absorption strengths and profiles between 2006 and 2007, the EWs measured in the two epochs were analyzed separately.

As noted in previous sections, the “core” and “wing” components of the line profiles show different behaviors as a function of line excitation energy, both in the observed ortho-para ratio of C_2H_2 absorption depths and in the interesting absence of a red wing in the Q-branch NH_3 lines. We therefore measured and analyzed the absorption as that of two velocity components, simply defined: one redward of $\sim 26 \text{ km s}^{-1}$ and the other blueward of the same velocity. A possible alternative would have been to decompose the profile into two Gaussians. However, because the

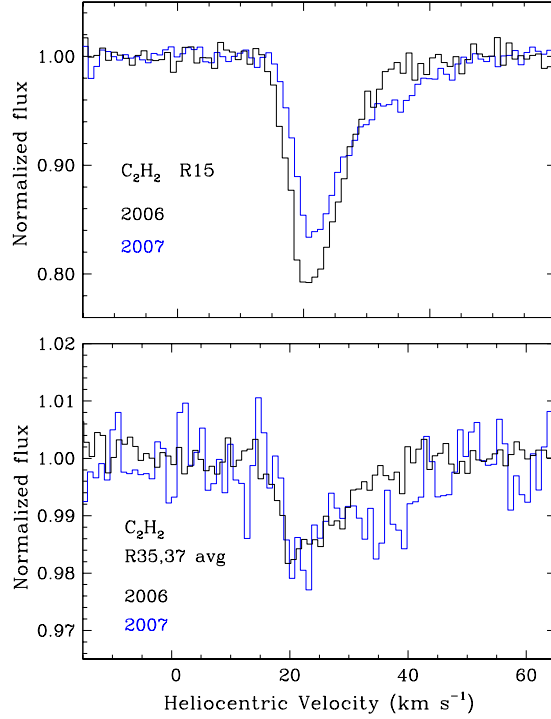


Fig. 11.— Comparison of profiles of high- J (top) and low- J (bottom) profiles of C_2H_2 lines in 2006 and 2007.

profiles are not strictly Gaussian, and they in fact appear to be composed of multiple components with possibly complex behavior, we adopted the simpler approach, with the goal of capturing the essence of the difference between the lower and higher velocity absorption.

The measured EWs for the two velocity components and their combined EW are given in Tables 3 and 4 for all lines measured in 2006 and 2007, respectively. The uncertainties include both the spectral pixel-to-pixel noise, which comes from the continuum signal-to-noise, and an estimate of the uncertainty in the continuum placement. The average line depth over the velocity interval is also listed for both components. In analyzing the detected H_2O absorption, we found it useful to also include upper limits on a few additional H_2O lines that could become detectable at very high column density and lower temperatures. These lines are listed in Table 4 along with their $2\text{-}\sigma$ upper limits on EW for the high-velocity component.

In the case of a uniform absorbing medium that lies in front of an opaque continuum source, the absorption equivalent width, which is a simple function of the line optical depth τ_ν , can be diluted by unobscured continuum emission (e.g., if the absorber does not completely cover the background MIR continuum source) and/or by emission from the absorber. That is, if the emission from a background source $B_{\nu,b}(T_b)$ with temperature T_b is absorbed by a medium with opacity τ_ν and source function $S_{\nu,a}$, the emergent intensity is

$$I_\nu = B_{\nu,b} e^{-\tau_\nu} + (1 - e^{-\tau_\nu}) S_{\nu,a} \quad (1)$$

at a frequency ν in the line and $I_\nu = B_{\nu,b}$ in the neighboring continuum. The fractional intensity decrement in the line relative to the continuum is then

$$(B_{\nu,b} - I_\nu) / B_{\nu,b} = (1 - e^{-\tau_\nu}) (1 - S_{\nu,a} / B_{\nu,b}), \quad (2)$$

and the equivalent width

$$EW = f_c \int (1 - I_\nu / B_{\nu,b}) d\nu = f_d \int (1 - e^{-\tau_\nu}) d\nu, \quad (3)$$

where the quantity

$$f_d = f_c (1 - S_{\nu,a} / B_{\nu,b}) \quad (4)$$

combines the effects of the covering fraction of the absorber f_c and the average dilution by emission from the absorber across the line $f_e = (1 - S_{\nu,a} / B_{\nu,b})$. In LTE, $S_\nu = B_\nu(T)$ where T is the temperature of the absorbing medium. However, as a result of the high critical density for vibrational LTE, the vibrational temperature T_{vib} may be less than T , and both S_ν and T_{vib} can be affected by the radiation field.

Here we model the absorbing gas as a uniform slab. The line optical depths are determined by the gas temperature (T), and the ratio of the column density of the molecule (N) to the intrinsic line width, which includes thermal and microturbulent components. If the absorption is approximated as a Gaussian line profile with FWHM $\Delta\nu$, the line center optical depth is

$$\tau_0 = \frac{g_u A \bar{\nu}^3}{8\pi} \frac{e^{-E_\ell/kT}}{Q(T)} \frac{N}{1.0645 \Delta\nu} (1 - e^{-hc\bar{\nu}/kT}) \quad (5)$$

where $\bar{\nu}$ is the wavenumber of the transition, g_u is the multiplicity of the upper state, E_ℓ is the energy of the transition, Q is the partition function, and the factor 1.0645 relates the product of the FWHM and peak height of a Gaussian to its area. All of the molecular parameters and data for the partition functions are from HITRAN (Rothman et al 2013; Fischer et al. 2003). We assume that the lower energy levels are in LTE.

For each molecule and velocity component, we plot a curve-of-growth (COG) as $\ln(EW)$ versus the logarithm of a quantity proportional to τ_0 and then determine the model parameters that minimize χ^2 . The first two parameters, T and $N/\Delta\nu$, determine the line optical depths and the shape of the COG; equivalently, these two parameters set the relative EWs of the lines. The third parameter in this approach, $f_d \Delta\nu$, is a scaling factor that best matches the absolute EWs for all lines. From these three parameters, the value of $f_d N$ automatically follows.

Note that f_d and $\Delta\nu$ are not independently determined, although it is possible to place physical limits on $\Delta\nu$ (and hence f_d). If all lines are optically thin (all points fall on the linear part of the COG), $N/\Delta\nu$ is not constrained and the only determined parameters are T and $f_d N$. The results from the COG analysis are given in Tables 5 and 6. The parameter uncertainties represent 1- σ , i.e., a 68% confidence interval, where the joint confidence region for the parameters is the space enclosed by the surface of constant χ^2 that corresponds to the confidence level and the number of

free parameters. Note that there is correlation between parameters, such that the upper bound on temperature generally corresponds to lower column density and larger intrinsic line width, and visa versa. The uncertainties depend on the number of lines used, the signal-to-noise of the EWs, and the range in optical depth and lower energy level covered by the measured transitions.

In Figure 12, example COGs are plotted for both the low- and high-velocity components of C_2H_2 from 2006. The COG analysis shows quantitatively the conclusion reached from visual examination of the C_2H_2 spectra; the high-velocity (HV) component (the red wing) has a higher optical depth than the low-velocity (LV) component (the 22 km s^{-1} core), as indicated by the greater curvature in its COG. The line with the highest opacity is the R15, which has an optical depth of 2 for the LV and 6 for the HV component. Remarkably, the temperatures of the HV and LV components are about the same, $\sim 450 \text{ K}$. Thus, our finding that higher rotational transitions are more prominent in the HV component is not due to a higher temperature for the high-velocity gas but to greater optical depth (larger $N/\Delta v$).

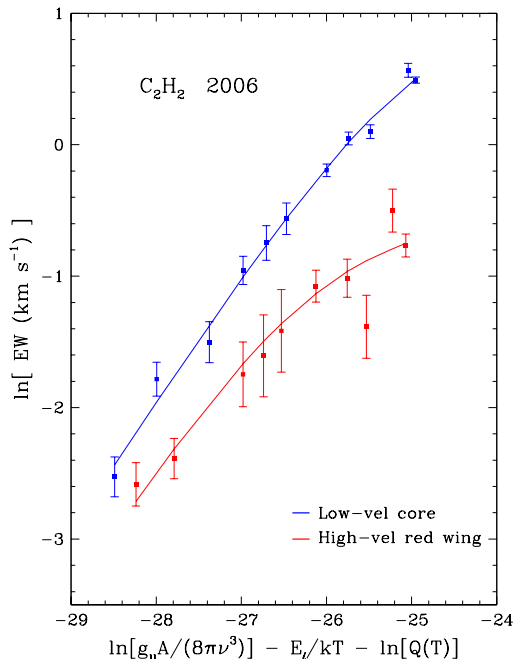


Fig. 12.— Curves of growth for the low-velocity (blue points) and high-velocity (red points) components of C_2H_2 in 2006. The solid lines are the best-fit model curves of growth.

Despite its higher optical depth, the EWs and absorption depths of the HV component are smaller than those of the LV component, indicating a larger dilution factor. Because the LV and HV components share the same temperature (Tables 5, 6), the contribution of line emission by the warm absorber to the value of f_d (through the quantity f_e in eq. 1) is the same for both components. Thus, the greater dilution of the HV component (i.e., smaller f_d) compared to the LV component indicates that the covering fraction of the background continuum is smaller for the high-velocity

gas than the low-velocity gas.²

For H₂O, the absorption is dominated by the HV component (Section 3.3); the observed redward velocity of the absorption shifts it out of the telluric water absorption, enabling its detection. The 20 km s^{−1} component is clearly detected in the average spectrum (Fig. 9), but it is too weak in individual lines to be useful in determining the absorption parameters. Therefore, the analysis was restricted to the HV component. Furthermore, because all four of the detected lines are optically thick, we are unable to constrain the absorption properties using these lines alone. We therefore also included in the analysis the upper limits on several additional water lines covered by our spectra. Because these additional lines, shown in Table 4, would become strong enough to detect at very high column density and/or low temperature, including their upper limits places an upper bound on the water column density. The 2- σ upper limits were included in the χ^2 fit using the approach discussed in Sawicki (2012). The best-fit COG for the H₂O absorption is shown in Figure 13. The resulting analysis yields the best-fit properties shown in Table 6.

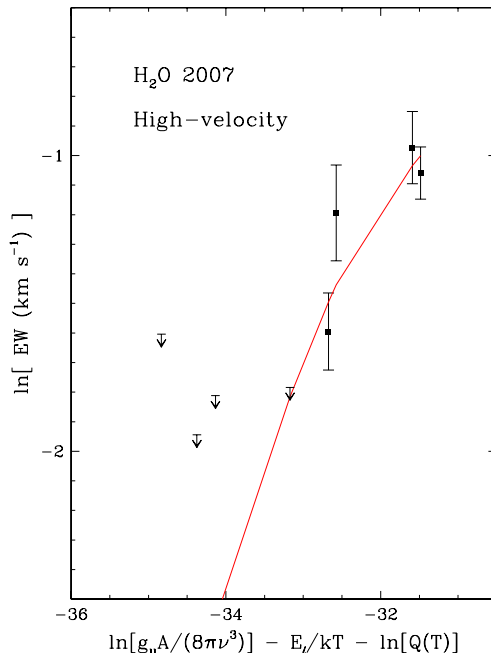


Fig. 13.— Curve of growth for H₂O. Detected water lines (solid points) and upper limits (downward arrows) are indicated along with the best fit (red line).

²Small values of f_d reflect small covering fractions rather than significant emission from the absorbing gas. The vibrational temperature of the absorber T_{vib} and the temperature of the background continuum T_b would have to be very similar for emission to have a significant impact. In LTE, T_{vib} is the same as the rotational temperature of the absorber, which is here ~ 450 K. For $T_{\text{vib}}=450$ K, reducing f_e to 0.16–0.21, the range of dilution factors inferred for the LV component (Tables 5 and 6), requires a background continuum temperature of $T_b=480$ –490 K. Such similar foreground and background temperatures seem implausible; with temperatures that similar, the foreground gas is as likely to produce emission as absorption.

Using the above procedure, we derived gas temperatures of ~ 450 K for both velocity components of all molecules, with one clear exception discussed below. For molecules other than water, the derived values for $N/\Delta v$ are in the range $10^{16} - 10^{17} \text{ cm}^{-2} \text{ km}^{-1} \text{ s}$, with the value for the HV component consistently 3–7 times greater than that for the LV component. For the HV component of water, $N/\Delta v$ is much larger, $2.9 \times 10^{19} \text{ cm}^{-2} \text{ km}^{-1} \text{ s}$.

Because radiative transitions between rotational levels of C_2H_2 are forbidden, collisions will control the rotational populations in the ground vibrational state. Therefore, LTE should be a good approximation for C_2H_2 and the derived temperature a measure of the gas kinetic temperature. For HCN, the critical densities for our measured transitions range from $10^8 - 10^9 \text{ cm}^{-3}$. The derived excitation temperature is the same as that of C_2H_2 (for the 2006 data), indicating that the gas densities are at least this high. The measured rotational levels for NH_3 have comparable critical densities. However, the critical densities for the measured water lines are higher, $\sim 4 \times 10^{10} \text{ cm}^{-3}$. Models of disk atmospheres predict that warm molecules are present at high densities ($\gtrsim 10^{11} \text{ cm}^{-3}$), making LTE a reasonable assumption (e.g., Bruderer 2014; Najita & Ádámkóvics 2017).

To determine the line-of-sight column density N from the constrained quantity $N/\Delta v$ requires an assumption about the local line broadening Δv . A lower limit on N comes from assuming that the local line broadening is thermal, which for the observed molecules is $\sim 1 \text{ km s}^{-1}$ at 450 K. For an upper limit to N , we can adopt for Δv the observed width of the absorption component ($\sim 8 \text{ km s}^{-1}$), which would be appropriate if the absorbing medium is highly turbulent. However, this is unlikely, because the profiles of the R15 and R14 lines of C_2H_2 are identical across the LV component, i.e., the ortho-para ratio and hence the optical depth is nearly constant across the LV core of the lines. If the absorption was due to a single intrinsically broad ($\sim 8 \text{ km s}^{-1}$) profile, then the optical depth would be highest at the absorption minimum and decrease away from line center, in contrast to the observed profiles.

More likely, the observed width of the absorption feature is produced by multiple lines of sight through the rotating disk atmosphere that pass through gas at different velocities. In this case, the local line broadening Δv is substantially less than the full observed width, implying a smaller line-of-sight column density. In Tables 5 and 6 we list values for N for an assumed width of 2 km s^{-1} , a value between the approximate thermal width of hydrogen (4.5 km s^{-1}) and that of water ($\sim 1 \text{ km s}^{-1}$) at the temperature of the absorption (450 K), implying some amount of microturbulent broadening for the observed molecules. We interpret these values of N in the next section.

Although we find a ~ 450 K temperature for the velocity components of almost all molecules, we derive a much lower temperature for NH_3 in 2007 (250 K) than in 2006 (455 K) for the LV component. Because the addition of the Q branch in the 2007 data adds a large number of lines, which cover a greater range in optical depth, the temperature from the COG is well constrained. Setting the temperature to 250 K for the 2006 data gives an extremely bad fit. One could be

concerned that the Q branch probes different gas, given its different behavior, i.e., the absence of the red wing in the Q-branch lines. In Figure 14, we plot the COG for the 2007 LV component, where the model COG is the best fit to the combined Q- and P-branch lines. The P-branch lines are plotted with a different color, and follow the same trend as the Q-branch lines. In addition, fitting the Q- and P-branch lines separately yields consistent temperatures.

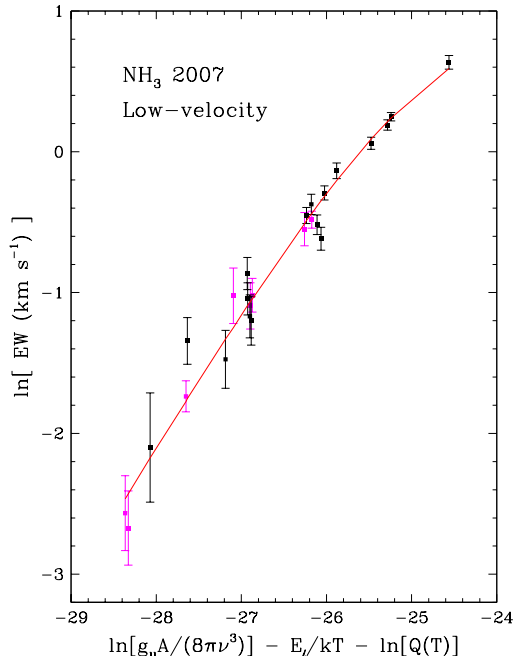


Fig. 14.— Curve of growth for the 2007 low-velocity component of NH_3 . The Q-branch (black) and P-branch (pink) lines follow the same trend and are fit with similar temperatures. The solid line is the best-fit model curve of growth.

Comparison with Previous Results. We can compare our results for HCN to the findings of Doppmann et al. (2008), who measured the $3\ \mu\text{m}$ absorption lines of HCN and C_2H_2 in GV Tau N at a resolution of $13\ \text{km s}^{-1}$ using NIRSPEC on Keck. They fit the ν_1 HCN spectrum with a temperature of 550 K and an HCN column density of $1.5 \times 10^{17}\ \text{cm}^{-2}$, using a microturbulent velocity of $3\ \text{km s}^{-1}$ ($\text{FWHM} = 5.0\ \text{km s}^{-1}$). This is equivalent to $N/\Delta v = 3 \times 10^{16}\ \text{cm}^{-2}\ \text{km}^{-1}\ \text{s}$. Hence, their result is in reasonable agreement with the values we obtained with the MIR lines for the LV component of HCN.

We can also compare the results from our spectrally resolved molecular spectra with the analysis by Bast et al. (2013) of the *Spitzer*/IRS spectrum of GV Tau. Our study differs from that of Bast et al. in two important ways. Firstly, the TEXES data spatially resolve the N and S components of the binary, whereas Bast et al. did not account for dilution by GV Tau S. Our TEXES observations confirm that the S component lacks MIR molecular absorption, a result similar to that found in *L*-band molecular spectroscopy of GV Tau N and S (Doppmann et al. 2008; Gibb et al. 2007). Secondly, the high spectral resolution of the TEXES data allows us to resolve the profiles and to infer dilution of the line equivalent widths.

For comparison to Bast et al., we use the $f_d N$ values from our analysis with $f_d = 1$, i.e., the column densities we would derive without taking dilution into account. For C_2H_2 and HCN, our column densities are somewhat larger, by factors of 1–3, than those reported by Bast et al. The temperature for HCN is in agreement, but their temperature for C_2H_2 (720 K) is higher. For NH_3 , our values of $f_d N \sim 2 \times 10^{16} \text{ cm}^{-2}$ are similar to the upper limit reported by Bast et al. ($1.9 \times 10^{16} \text{ cm}^{-2}$ for 500 K). All of our derived column densities would be larger for $f_d < 1$. Some of the observed differences may be due to variability, because the *Spitzer* and TEXES data were taken at different times.

To summarize, the TEXES spectra reveal warm ($\sim 450 \text{ K}$), redshifted MIR molecular absorption in GV Tau N, with larger column densities than inferred in previous studies. The HV component of the absorption is more optically thick than the LV component, has a column density 3–6 times larger, and is more highly diluted (by a factor ~ 5) than the LV component due to a smaller covering fraction of the background MIR continuum.

4. Discussion

4.1. Origin of the Absorption

The working hypothesis in the literature is that the molecular absorption in GV Tau N occurs in gas in the disk atmosphere observed against the hotter dust continuum from smaller radii in a disk viewed close to edge-on (Gibb et al. 2007; Doppmann et al. 2008; Bast et al. 2013). Here we discuss the origin of the absorbing gas in light of our results on the temperature, column densities, and line profiles of the molecular absorption.

Clues from Temperature and Column Density. We find that the absorbing gas is warm ($\sim 450 \text{ K}$) and the detected molecular species show profiles that can be modeled as multiple velocity components that probe gas along the same lines of sight to the $12 \mu\text{m}$ continuum. The rotational temperatures derived for the HCN, C_2H_2 , and H_2O absorption are similar to (but at the cool end of) the excitation temperatures derived for the same molecules from the MIR molecular emission observed from T Tauri disks (400–1000 K; Carr & Najita 2011; Salyk et al. 2011). The latter is thought to arise from the heated disk atmosphere within an au of the star (e.g., Najita et al. 2011; Najita & Ádámkóvics 2017).

The relative column densities of the molecular species detected in absorption in GV Tau N are also consistent with the ratios derived for the MIR molecular emission from T Tauri disks. For the high-velocity absorption component measured for GV Tau N in 2007, for which a H_2O column density could be determined, the column density ratios are $N(\text{C}_2\text{H}_2)/N(\text{H}_2\text{O}) = 0.002$, $N(\text{HCN})/N(\text{H}_2\text{O}) = 0.005$, and $N(\text{C}_2\text{H}_2)/N(\text{HCN}) = 0.4$. Figure 15 compares the GV Tau N column density ratios (blue star) with the emission column density ratios of T Tauri disks derived from high and low resolution spectra (squares). The GV Tau N values are similar to the ratios

derived from T Tauri star emission spectra using slab models that make assumptions similar to those adopted here. The similar column density ratios are consistent with the interpretation that the GV Tau N absorption arises in a disk atmosphere.

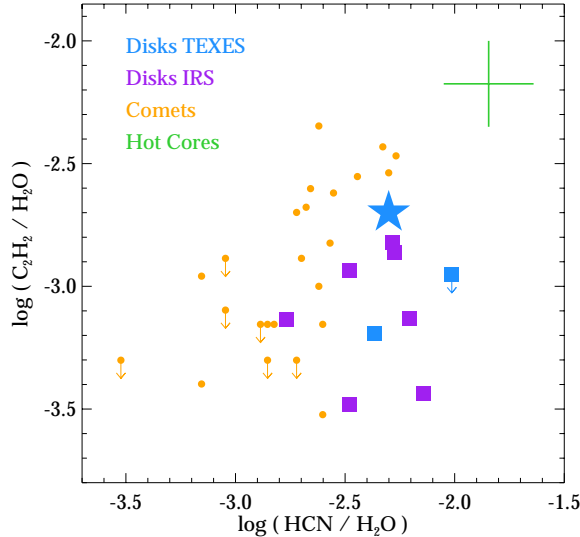


Fig. 15.— Molecular absorption column density ratios reported here for GV Tau N (blue star) compared with emission column density ratios from T Tauri disk spectra studied at high spectral resolution with TEXES (blue squares; Najita et al. 2018) and low spectral resolution with *Spitzer*/IRS (purple squares; Carr & Najita 2011; Najita et al. 2018). The estimates from *Spitzer* assume equal emitting areas for all molecules. Also shown are the abundances of comets (orange dots; Dello Russo et al. 2016), and the average properties of hot cores (green cross; see Carr & Najita 2011 for details). The GV Tau N absorption column density ratios are similar to the emission column density ratios of T Tauri disks, consistent with the interpretation that the absorption arises in a disk atmosphere viewed at high inclination.

At the same time, the absolute column densities of the MIR absorption are much higher than the column densities seen in emission. Here we compare specifically to results for AS205 N and DR Tau, two high accretion rate disks viewed at low inclination. As the only sources whose HCN and C₂H₂ emission has been measured at high spectral resolution, their velocity-resolved spectra enable tighter constraints on the properties of the emitting gas (Najita et al. 2018). For a valid comparison (apples to apples), we assume thermal local linewidths for the GV Tau N absorption, as assumed in the earlier emission line analysis. The column densities of H₂O, HCN, and C₂H₂ in the HV absorption component of GV Tau N are 40 times greater on average than the emission column densities of AS205 N and DR Tau, and the (HCN and C₂H₂) column densities of the LV component of GV Tau N are ~ 10 times greater. The roughly order-of-magnitude larger line-of-sight column densities observed in absorption vs. emission are expected if the warm molecular layer responsible for the T Tauri star emission is viewed at high inclination in GV Tau N, as in an edge-on disk.

There is little definitive information available on the orientation of the GV Tau N disk. Modeling of MIR interferometric observations made with VLTI/MIDI favored a high inclination for GV Tau N ($i \sim 80$ degrees; Roccatagliata et al 2011). In addition, the CO overtone emission from

the inner disk of GV Tau N is broad ($\sim 95 \text{ km s}^{-1}$) suggesting the disk is not close to face on (Doppmann et al. 2008). In contrast, modeling that fits the spectral energy distribution (SED) and scattered light images of GV Tau N with a disk + envelope model favors a lower inclination ($i \sim 30$ degrees; Sheehan & Eisner 2014). However, the SED modeling may not provide a strong constraint on the orientation of the inner disk of GV Tau N; because the modeling weights large-scale phenomena prominently in the fit, the preferred solution may be influenced primarily by the envelope properties rather than the inner disk ($< 10 \text{ au}$) properties where the warm absorption arises.

Clues from Line Profiles. While the results above echo previous results from the literature, the high velocity resolution of the TEXES data lends new insights into the dynamics of the absorbing gas. The $R=600$ *Spitzer* spectra detected molecular bands but did not resolve individual lines. The NIRSPEC/Keck spectra studied by Doppmann et al. (2008) and Gibb et al. (2007) marginally resolved individual HCN lines in the L -band. In comparison, the TEXES data, with a resolution of $\sim 3 \text{ km s}^{-1}$, measure the profiles of individual lines.

In interpreting the line profiles, we adopt as the system velocity for GV Tau N the velocity measured for the gaseous envelope surrounding GV Tau ($v_{\text{helio}} = 17.3 \pm 0.5 \text{ km s}^{-1}$ or $v_{\text{LSR}} = 7.0 \text{ km s}^{-1}$; Hogerheijde et al. 1998). The stellar radial velocity of GV Tau N is not well known. One estimate, based on an absorption component detected in the CO overtone emission from the source ($v_{\text{helio}} = 5.8 \pm 4.0 \text{ km s}^{-1}$), is blueshifted relative to both the cloud and envelope velocity, suggesting that the central source may be a spectroscopic binary (Doppmann et al. 2008).

As described in Section 3, the GV Tau N line profiles have single-dipped, $\sim 10 \text{ km s}^{-1}$ FWHM absorption line profiles; the absorption core has a velocity offset redward of the system velocity and a red wing extending to higher velocities. The redward offset of the core and red wing are not expected for a simple rotating disk and suggests gas that is radially inflowing. The redshifted absorption we observe is reminiscent of earlier Keck/NIRSPEC results for GV Tau N. Doppmann et al. (1998) found that the NIR HCN absorption toward GV Tau N, centered at 19 km s^{-1} , is $\sim 2 \text{ km s}^{-1}$ redward of the system velocity.

Assuming that all of the absorbing gas resides at $\sim 19 \text{ km s}^{-1}$, Doppmann et al. (2008) argued that the NIR warm molecular absorption is unlikely to arise from gas in an infalling envelope. Given the inferred mass of the stellar component(s) of GV Tau N ($0.8 M_{\odot}$), the envelope infall velocity $v_{\text{in}} = (2GM_{\star}/r)^{1/2}$ would reach the observed 2 km s^{-1} velocity shift at a distance of 360 au . In contrast, models of infalling protostellar envelopes predict that the gas temperature reaches 500 K only within 2 au of the star at the $\sim 7 L_{\odot}$ accretion luminosity of GV Tau (Ceccarelli et al. 1996, their Fig. 4), i.e., well within the distance of 360 au that would be inferred for the infalling gas based on its velocity relative to the molecular envelope. If the NIR molecular absorption arises in infalling gas at 360 au , an additional, non-traditional source of heating is needed to explain the observed temperature of the absorbing gas.

A similar argument applies to the MIR absorption. At the higher resolution and signal-to-noise of the TEXES spectrum compared to the NIRSPEC results, we find that the core of the

MIR molecular absorption, centered at 21–22 km s^{−1}, is ~ 4 km s^{−1} redward of the system velocity, with the red wing of the absorption extending to larger velocities, $\sim 15 - 20$ km s^{−1} redward of the system velocity. Infalling gas would reach the ~ 4 km s^{−1} redshifted velocity of the absorption core at ~ 90 au and the ~ 17 km s^{−1} wing velocity at ~ 5 au from an $0.8M_{\odot}$ star. While some of the high velocity gas (arising within ~ 10 au) might be warm enough to explain the observed absorption, the bulk of the infalling gas at ~ 90 au would be too cool to explain the observed absorption.

Moreover, because of angular momentum conservation, it may be very difficult for infall to reach the inner few au of a Class I system. For rotating infall, angular momentum prevents direct accretion onto the star and its vicinity, instead causing the infalling material to reach the disk near the centrifugal radius (20–40 au). The difficulty of reaching the inner few au through infall is even more true for late accretion sources in which the infall is increasingly dominated by high angular momentum material. GV Tau, which has a weak molecular envelope, is such a late accretion source, i.e., transitioning from a Class I source to a Class II source.

Another general argument against infall (and in favor of an inner disk atmosphere) is the molecular composition of the absorption and its rarity. Figure 15 shows that the GV Tau ratios of C₂H₂, HCN, and water are similar to those of T Tauri disk atmospheres seen in emission. Such absorption is rare. GV Tau N is the only Class I source known to show C₂H₂, HCN, water, and NH₃ in absorption. One other source shows C₂H₂ and HCN absorption in its *Spitzer* spectrum (IRS46; Lahuis et al. 2006).

If the temperature and composition we observe in GV Tau N were typical of infalling envelopes, we would commonly observe these features in Class I sources. Compared to a disk atmosphere, gas in an infalling envelope would cover a much larger fraction of the star, approximately the range of polar angles between the disk surface and the inner cavity carved out by outflow. As a result, absorption from infall would be detected over a much wider range of viewing angles than disks viewed nearly edge on. The rarity of molecular absorption like that seen in GV Tau N argues against its origin in an infalling envelope.

Disk Origin. Unlike the infalling envelope scenario, a nearly edge-on rotating disk can account for almost all of the properties of the observed molecular absorption: the temperature and column density (as discussed above) and its line width. Single-dipped absorption line profiles can arise when a disk atmosphere is seen in absorption against the MIR continuum arising from smaller radii. While both the line absorption and the continuum emission likely arise over a range of radii, for simplicity in the discussion below, we assume that the continuum arises from a compact region $r < r_c$, and the absorption occurs at larger radii $r_a > r_c$. Because the MIR continuum is compact compared to r_a , only the portion of the disk atmosphere at r_a that is close to the line-of-sight to the continuum is seen in absorption, i.e., within an azimuthal angle $\pm\phi$ where $\sin\phi = r_c/r_a$ (Fig. 16)

Gas at r_a along the line-of-sight to the MIR continuum has a maximum projected radial velocity of $v_{los} = \pm v_a \sin\phi \sin i$ where v_a is the disk rotational velocity at r_a and i is the disk inclination. For a disk in Keplerian rotation, where the projected radial velocity due to rotation

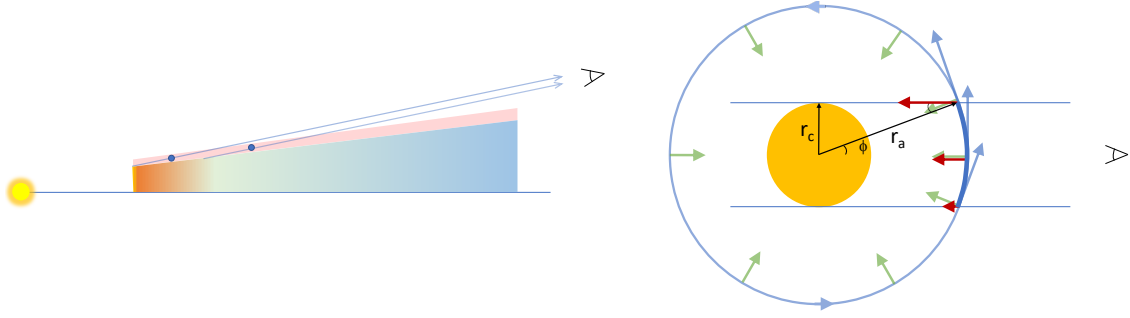


Fig. 16.— *Left*: Schematic (not to scale) illustrating the likely observing geometry of GV Tau N. The line of sight to the MIR disk continuum (orange region) passes through the warm molecular atmosphere at larger radii (pink region), producing molecular absorption that samples a range of radii in the atmosphere (between the blue dots). *Right*: Top down view of the warm molecular absorption velocities. Absorption by gas at a given radius r_a (heavy blue arc) along the line of sight to the warmer MIR continuum at $r < r_c$ (yellow-orange region) has velocity components from both rotation (blue arrows) and inflow (green arrows). The absorption velocities (red arrows) are shifted to the red and span a range of velocities.

at r_c is v_c and the projected radial velocity at r_a is $v_a = v_c (r_c/r_a)^{1/2}$, $v_{los} = \pm v_c \sin i (r_c/r_a)^{3/2}$. If the $12 \mu\text{m}$ continuum arises within $r_c = 0.3 \text{ au}$ of the star, where $v_c = 49 \text{ km s}^{-1}$ for an $0.8 M_\odot$ star, maximum absorption velocities of $v_{los} = \pm 5 \text{ km s}^{-1}$ would arise at a modestly larger radius of $r_a = 1.4 \text{ au} (\sin i)^{2/3}$. (That is, gas at this radius would absorb background continuum emission from $\sim 0.3 \text{ au}$ over the 10 km s^{-1} FWHM of the observed absorption features.) Higher velocity absorption would arise from gas at smaller radii. Lower velocity absorption arises from both gas at larger radii as well as gas at smaller radii that are close to the line of sight to the star. At a disk radius of 4 au , the maximum absorption velocity would be $\pm 1 \text{ km s}^{-1} (\sin i)$.

Thus, a conventional rotating, edge-on disk can account for almost all of the properties of the observed molecular absorption (the temperature, column density, and its line width), except for its redshift from the system velocity. We can also account for the redward offset of the absorption core if the gas in the disk atmosphere is also radially inflowing along the disk surface (Fig. 16). Such “surface accretion” flows are found in simulations of rotating magnetized disks.

4.2. Surface accretion in GV Tau N?

In their global ideal MHD simulations of thin disks threaded by a vertical magnetic field, Zhu & Stone (2018) found that accretion occurs primarily in a surface accretion flow in the upper, magnetically dominated disk surface. (See also earlier theoretical work by Stone & Norman 1994; Beckwith et al. 2009; Guilet & Ogilvie 2012, 2013.) The accretion is supersonic, reaching inward velocities $v_r = 2\text{--}4 c_s$ where c_s is the sound speed.

In their simulation, the rapid accretion at the disk surface (primarily due to the magnetic $B_r B_\phi$ stress) carries the magnetic field inward, pinching it inward at the disk surface. As a result, the disk atmosphere is connected magnetically to the midplane at larger radii, which spins down the atmo-

sphere, producing significantly sub-Keplerian rotation—as small as 60% of Keplerian rotation—in the atmosphere. The inward pinching of the magnetic field also launches a disk wind, although the torque due to the wind at the disk surface plays only a small role in driving accretion.

The expected properties of the accreting atmosphere are roughly consistent with the observed properties of the molecular absorption in GV Tau N. For molecular gas at 500 K, supersonic accretion at $v_r = 2\text{--}4 c_s$ corresponds to $v_r \simeq 3\text{--}5$ km/s, qualitatively similar to the redshift of the absorption core (~ 4 km/s); the velocities of the red wing ($\sim 15\text{--}20$ km/s) correspond to higher velocities $\sim 13c_s$. For gas in sub-Keplerian rotation at a disk radius r_a along the line of sight to the MIR continuum (which arises within r_c), its projected radial velocity spans the range $v_{los} = \pm \beta \sin i v_c (r_c/r_a)^{3/2}$, as described above, where β is a factor that accounts for possible deviations from Keplerian rotation. If $\beta = 0.6$ and $r_c = 0.3$ au so that $v_c = 49$ km s $^{-1}$ for a stellar mass of $0.8M_\odot$, an observed absorption core with a FWHM of ± 5 km s $^{-1}$ would correspond to absorbing gas at $r_a = 1$ au $(\sin i)^{2/3}$.

Preliminary work on a detailed radiative transfer model of a rotating disk with radial inflow, viewed nearly edge on, appears to be able to account for the properties of the molecular absorption observed in the GV Tau N spectrum. The modeling, which builds on the previous results of Lacy (2013), can plausibly account for the shape of the absorption components as well as the slightly blueshifted emission seen in the NH $_3$ P-branch profiles. In one promising scenario, rapidly inflowing gas near the inner rim of the disk is seen against the continuum from the inner rim, and more slowly inflowing gas located near the disk surface at larger radii is seen against the disk continuum at smaller radii (Lacy et al., in preparation).

If the observed absorption arises in a surface accretion flow, the flow may carry a significant mass accretion rate. For an inward flow with velocity v_{in} and vertical column density N_\perp at a characteristic radius r_a , the mass accretion rate is

$$\dot{M}_{\text{abs}} = 2\pi r_a m_H v_{in} N_\perp. \quad (6)$$

If we assume

$$N_\perp = N_{\text{abs}} \eta / x_{\text{mol}} \quad (7)$$

where N_{abs} is the observed line-of-sight molecular absorption column (e.g., values in the final column in Tables 5 and 6), η is the ratio of the vertical to the line-of-sight molecular column densities, and x_{mol} is the abundance of the tracer molecule relative to hydrogen, the associated accretion rate is

$$\dot{M}_{\text{abs}} = 10^{-9} M_\odot \text{ yr}^{-1} \left(\frac{v_{in}}{4 \text{ km s}^{-1}} \right) \left(\frac{N_{\text{abs}}}{10^{16} \text{ cm}^{-2}} \right) \left(\frac{r_a}{1 \text{ au}} \right) \left(\frac{\eta}{0.1} \right) \left(\frac{x_{\text{mol}}}{10^{-6}} \right)^{-1}. \quad (8)$$

For the observed HCN absorption, the properties of its LV component are $v_{in} = 4$ km s $^{-1}$, $N_{\text{abs}} = 7 \times 10^{16}$ cm $^{-2}$. Assuming an abundance in the warm disk atmosphere of $x_{\text{HCN}} \sim 10^{-6}$ at ~ 1 au, as found in disk chemistry models that account for the MIR molecular emission properties of T Tauri disks (Najita & Ádámkóvics 2017), and $\eta = 0.1$, the corresponding vertical column density and accretion rate are $N_\perp = 7 \times 10^{21}$ cm $^{-2}$ and $\dot{M}_{\text{abs}} \sim 7 \times 10^{-9} M_\odot \text{ yr}^{-1}$.

Similarly, given the inferred properties of the HV HCN absorption component, $v_{\text{in}} = 20 \text{ km s}^{-1}$, $N_{\text{abs}} = 3 \times 10^{17} \text{ cm}^{-2}$, the corresponding vertical column density is $N_{\perp} = 3 \times 10^{22} \text{ cm}^{-2}$, and the accretion rate associated with the HV component is 20 times larger than that of the LV, or $\dot{M}_{\text{abs}} \sim 1.5 \times 10^{-7} M_{\odot} \text{ yr}^{-1}$. Using the properties of the HV water absorption ($N_{\text{abs}} = 5.8 \times 10^{19} \text{ cm}^{-2}$) and a conservative water abundance estimate of $x_{\text{H}_2\text{O}} \sim 3 \times 10^{-4}$ (Najita & Ádámkóvics 2017) yields a similarly large estimate of the accretion rate of the HV component, $1 \times 10^{-7} M_{\odot} \text{ yr}^{-1}$.

In adopting abundances for this estimate, we want to select values from model atmospheres that are able to match the properties of the *Spitzer* molecular emission from inner disks and use abundance values appropriate for the warm atmosphere region that is responsible for the emission. The models in Najita & Ádámkóvics (2017) do a fair job reproducing the properties of many of the molecules detected with *Spitzer*. To make a conservative estimate of the accretion rate, we have adopted model abundances at the high end of the predicted values within the layer responsible for the emission. The properties of the Walsh et al. (2015) and Voitke et al. (2018) models differ from those of Najita & Ádámkóvics in detail (e.g., the molecular atmosphere of Voitke et al. is much cooler), but their model abundances, if adopted, would imply similar or larger accretion rates. For example, Walsh et al. find a peak HCN abundance of $\sim 10^{-7}$ which would imply a much larger accretion rate for the LV component of $\dot{M}_{\text{abs}} \sim 7 \times 10^{-8} M_{\odot} \text{ yr}^{-1}$. The peak water abundances for all of the models are similar $\sim 10^{-4}$. Thus, the molecular abundances of current disk atmosphere models suggest large accretion rates for both the LV and HV components.

The assumed value of $\eta = 0.1$ is plausible for the geometry of a highly inclined disk viewed close to edge on. A more accurate value could be obtained from a more complete model of the physical, thermal, and chemical disk conditions.

The above discussion assumed a local line broadening of 2 km s^{-1} (Tables 6 and 7) and that the full absorption width we measure is actually the result of observing absorption along multiple lines of sight through the rotating disk atmosphere, encountering gas at different projected velocities. The column densities and accretion rates above would be smaller by a factor of two, or larger by a factor of 4, if we assumed that the local line broadening is instead thermal width or the full observed width of the absorption component, respectively.

The resulting vertical column densities ($7 \times 10^{21} \text{ cm}^{-2}$ for LV; $2 \times 10^{22} \text{ cm}^{-2}$ for HV) are similar to and larger than the vertical column densities thought to be responsible for the emission from T Tauri disks. The resulting accretion rates ($7 \times 10^{-9} M_{\odot} \text{ yr}^{-1}$ for LV; $1 \times 10^{-7} M_{\odot} \text{ yr}^{-1}$ for HV) span the range observed from typical to very active T Tauri stars. While there are substantial uncertainties associated with the above estimates (including the fact that we only measure gas columns where the molecular tracers are abundant and atomic gas is not probed), the inferred accretion rates are substantial and fall within the expectations for T Tauri stars. Thus, the observed radial inflow does appear capable of explaining the observed accretion rates of very active T Tauri stars and Class I objects.

The idea of accretion at the disk surface dates back at least to Gammie (1996), who described

a “layered accretion” picture of T Tauri disks, in which only the surface region of the disk that is sufficiently ionized to couple to magnetic fields participates in accretion via the magnetorotational instability (the “active layer”), and the deeper layers of the disk are a non-accreting “dead zone.” In Gammie (1996), the active layer was $\sim 100 \text{ g cm}^{-2}$ thick, and an equivalent viscosity parameter $\alpha = 0.01$ was sufficient to account for observed T Tauri stellar accretion rates ($\sim 10^{-8} M_{\odot} \text{ yr}^{-1}$). In the intervening years, more detailed models of disk ionization and our improved understanding of the role of non-ideal MHD processes have shrunk theoretical expectations for the vertical extent of the accreting layer to smaller and smaller column densities, requiring larger equivalent values of α and larger inflow velocities to deliver the same accretion rate. Here T Tauri-like accretion rates appear to be transported over vertical columns of only $\sim 0.01 \text{ g cm}^{-2}$.

Supersonic surface accretion flows—which differ from previous disk accretion mechanisms in that accretion is driven not by turbulence or a wind, but primarily by large-scale net magnetic fields in the disk atmosphere (Zhu & Stone 2018)—may help resolve the open question of how protoplanetary disks accrete at planet formation distances ($\sim 0.3\text{--}10 \text{ au}$). Because of the low ionization fractions of disks below their surfaces, it is increasingly unclear whether turbulence generated by the magnetorotational instability (MRI) can drive a significant accretion rate in protoplanetary disks (e.g., Turner et al. 2014).

The apparent evidence for a supersonic surface accretion flow in the disk of GV Tau N suggests an alternative pathway for disk accretion. As a mechanism that redistributes angular momentum within the disk rather than removing it from the system—as in a disk wind—the supersonic surface accretion flows studied by Zhu & Stone (2018) contribute to disk spreading: angular momentum from the disk surface is transported to the midplane at larger radii, which induces the surface to accrete and the midplane to spread to larger radii. As an “in-disk” transport mechanism, such surface accretion flows may help explain the larger sizes of gas disks surrounding Class II sources (as large as $\sim 500\text{--}800 \text{ au}$) compared to those of Class I sources (typically $< 100 \text{ au}$). The striking size difference has been interpreted as evidence that some “in disk” angular momentum transport process is active in the Class II (T Tauri) phase (Najita & Bergin 2018).

Our results may also be related to magnetothermal wind-driven accretion. Because the winds rely on relatively weak magnetic fields, their magnetic lever arms are small; as a result, transporting disk material from large radii to small (over a factor of 30 in radius, from 10 au to 0.3 au) is an inefficient process requiring large wind mass loss rates, comparable to or greater than the accretion rate (Bai & Stone 2013). Although strong observational evidence for such massive, angular momentum-removing disk winds is currently lacking, the winds are also predicted to produce accretion in narrow current sheets, which can reach high velocities near the disk surface under certain conditions (Bai 2013). If the net vertical field is anti-aligned with disk rotation, near-sonic to supersonic inflow can develop on one side of the disk surface over some range of radii; under other conditions, the accretion flow reaches much lower velocities or occurs close to the midplane (Bai & Stone 2013, Bai 2017). The accretion flow we observe in GV Tau N may be related to the predicted high-velocity flows.

Thus, our spectroscopic results appear to capture disk accretion in action and provide observational support for supersonic surface accretion, a potentially important mode of accretion in protoplanetary disks. To explore this possibility further, we need future spectroscopic searches for redshifted warm molecular absorption from other Class I sources; the incidence rate of the absorption, which constrains its covering fraction, can distinguish between an origin in a disk atmosphere (small covering fraction) or an infalling envelope (large covering fraction). Detailed radiative transfer (RT) modeling is needed to understand whether the line profiles we observe can actually be produced in disk atmospheres undergoing surface accretion. Similarly, thermal-chemical-RT modeling of infalling envelopes is needed to explore that alternative scenario as an explanation for the observed line profiles.

In addition, future theoretical work is needed to understand whether surface accretion flows can be driven under realistic ionization conditions in protoplanetary disks; the Zhu & Stone (2018) simulations were carried out assuming ideal MHD. At the observed inflow velocities of $\sim 5 \text{ km s}^{-1}$, the accreting material will travel an au in a year, implying that the flow must be rapidly replenished in order to sustain it over protostellar lifetimes ($\sim 10^5 \text{ yr}$). Whether and how the replenishment occurs—from disk inflows at larger radii and/or from deeper in the disk—is an open question. The results reported by Fuente et al. (2020) may provide a clue. They find evidence for redshifted absorption at modest inflow velocities ($\lesssim 3 \text{ km s}^{-1}$) in cool molecular gas at larger distances from GV Tau N, as traced in ^{13}CO (J=3-2).

It would also be useful to obtain additional observational evidence for surface accretion flows. As discussed above, even if disks do commonly accrete through their sub-Keplerian surfaces at supersonic speeds, such flows are unlikely to be commonly observed. Nearly edge-on disks, like that inferred for GV Tau N, are advantageous systems in which to search for surface accretion flows because the modest inward motions (few times the sound speed) are more readily detected from that viewing angle. However, edge-on disks are intrinsically rare because of their special orientation. Consistent with this picture, GV Tau N is one of the few YSOs to show molecular absorption in *Spitzer*/IRS spectra, and yet its SED is similar to that of other Class I sources (Furlan et al. 2008). That is, GV Tau N appears to be a typical Class I source viewed at an unusual inclination.

Although GV Tau N is rare in its molecular absorption properties, radial inflows have been reported in several other disk systems. As described by Zhang et al. (2015), the classical T Tauri star AA Tau, whose inner disk is highly inclined ($\sim 70\text{--}75$ degrees), shows very broad CO fundamental emission lines, with narrow absorption superposed near the line center. Following a photometric dimming event in 2011, the molecular absorption component increased in strength and showed a constant redshift of $\sim 6 \text{ km s}^{-1}$ with respect to the star. The observed velocity shift, temperature of the absorbing gas ($\sim 500 \text{ K}$), and inferred column density of the absorber ($N_{\text{H}} \sim 3 \times 10^{22} \text{ cm}^{-2}$) are comparable to the properties of the absorption in GV Tau N.

Perhaps most dramatically, Boogert et al. (2002) reported redshifted absorption in the $5 \mu\text{m}$

CO absorption spectrum of the Class I protostar L1489 IRS. The CO spectrum revealed redshifted absorption profiles similar to those seen here, but with a red wing extending to 100 km s^{-1} produced by warm ($\sim 250 \text{ K}$) gas. The absorption was interpreted as inward flowing gas at the warm disk surface, although at the time the phenomenon was reported, the physical origin of the gas was unclear. It is tempting to speculate that the CO absorption in L1489 IRS also arises in a disk surface accretion flow, albeit one with a very high inflow velocity.

As another possible example of a surface accretion flow but on a larger scale, spatially resolved CO $J=3-2$ imaging with ALMA of the Herbig Ae star HD100546 shows deviations from Keplerian rotation which have been interpreted as indicating either a severely warped and twisted inner disk or radially infalling gas within 100 au (Walsh et al. 2017). The lack of evidence for a disk warp from high contrast imaging of the dust disk favors the latter explanation. To explain the CO spatial and spectral structure, the required inward velocities are several times the sound speed, similar to the inflow speeds found in simulations that report surface accretion flows (Zhu & Stone 2018). Walsh et al. found reasonable fits to the HD100546 data with a radial flow that is 63% of the Keplerian velocity within 84 au. Given the $\sim 4.6 \text{ km s}^{-1}$ Keplerian velocity of HD100546 at 84 au (assuming a $2M_{\odot}$ star), the radial flow velocity is 2.6 km s^{-1} . If the gas temperature in the disk atmosphere at 84 au is 30 K, the expected inward flow velocity from a surface accretion flow is approximately $4c_s = 2.2 \text{ km s}^{-1}$, similar to the radial flow velocity inferred from the observations.

Similarly, ALMA imaging of HCO^+ emission from the classical T Tauri star AA Tau has a twist (within the innermost ring at 40 au) in the projected velocity field relative to the velocity field at larger radii, which is also interpreted as a warp or an inward radial flow (Loomis et al. 2017). Thus, although radial inflows have not been much reported to date, studies of detailed disk dynamics with ALMA and high resolution studies of nearly edge-on disks, carried out for larger samples than have been explored to date, can clarify this picture.

Another way to detect surface accretion flows may be through their sub-Keplerian rotation. While disk rotation at planet formation distances ($< 10 \text{ au}$) has been demonstrated using velocity-resolved molecular emission line profiles (e.g., CO fundamental emission), demonstrating that the rotation is sub-Keplerian requires spatial constraints on the observed velocities (i.e., spatially and spectrally resolved emission or spectroastrometry; e.g., Pontoppidan et al. 2011) as well as *independently determined* stellar masses. The latter may be challenging to obtain. One of the “gold standard” methods for measuring pre-main-sequence stellar masses is to spatially resolve the rotation of outer disks assuming pure Keplerian rotation (e.g., Simon et al. 2000).

4.3. First Detection of NH_3 in an Inner Disk?

Although ammonia has been previously reported in the outer disk of one young star (TW Hya, in data taken with the *Herschel Space Observatory*; Salinas et al. 2016), it has not been previously reported in inner disks, in either emission or absorption. In their analysis of *Spitzer* molecular

emission spectra taken at low resolution, Salyk et al. (2011) reported upper limits on the column density of ammonia, based on simple slab modeling and an assumed temperature of 400 K. The results correspond to upper limits on the ratio of ammonia to water of $[\text{NH}_3/\text{H}_2\text{O}] \lesssim 0.005$. The analysis by Bast et al. (2013) of the *Spitzer* absorption spectrum of GV Tau led to an upper limit on its NH_3 absorption column density of $2 \times 10^{16} \text{ cm}^{-2}$ assuming a temperature of 500 K. Our measured absorption columns for NH_3 towards GV Tau N are consistent with these upper limits.

Ammonia upper limits have also been derived from high resolution spectra of inner T Tauri disks. Mandell et al. (2012) reported upper limits on warm NH_3 emission corresponding to $[\text{NH}_3/\text{H}_2\text{O}] \lesssim 0.2$, based on VLT/CRIRES spectra at $3 \mu\text{m}$. Summarizing the results of a Gemini/TEXES program to search for NH_3 Q-branch emission at $10.75 \mu\text{m}$ from inner T Tauri disks, Pontoppidan et al. (2019) found a lower average abundance upper limit of $[\text{NH}_3/\text{H}_2\text{O}] < 0.003$. When compared with the HCN abundance measured in the same disks, the NH_3 upper limit corresponds to $[\text{NH}_3/\text{HCN}] < 0.1$.

Here we find a much larger $[\text{NH}_3/\text{HCN}]$ ratio for GV Tau N, which shows comparable absorption column densities in NH_3 and HCN. Using the best constrained values, that of $f_d N$ for the low velocity component of each molecule at each epoch, our inferred ratio of $[\text{NH}_3/\text{HCN}]$ is ~ 0.5 , much larger than the $[\text{NH}_3/\text{HCN}] \sim 0.1$ upper limits obtained by Pontoppidan et al. (2019) from the molecular emission spectrum of three T Tauri disks.

Whereas conspicuous NH_3 emission is absent in the *Spitzer* IRS spectra of T Tauri stars (e.g., Salyk et al. 2011, Carr & Najita 2011), detectable emission is expected if NH_3 is co-located with the HCN (i.e., has the same temperature; $\sim 600 \text{ K}$ in emission) and has an abundance similar to that of HCN. To illustrate this discrepancy, we show in Figure 17 examples of predicted molecular emission spectra for simple slab models of T Tauri disks. The predictions adopt the HCN column densities that have been derived for these disks assuming that the HCN emission has the same temperature and emitting area as the H_2O emission (Carr & Najita 2011; Najita et al. 2018). At the GV Tau N column density ratio of $[\text{NH}_3/\text{HCN}] = 0.5$ and a temperature of 600 K, the resulting NH_3 emission would be measureable (solid red line). At the lower ratio of $[\text{NH}_3/\text{HCN}] = 0.1$, corresponding to the high-resolution limits from Pontoppidan et al. (2019), the NH_3 emission would not be detectable (blue line).

The much higher $[\text{NH}_3/\text{HCN}]$ column density ratio observed in absorption GV Tau N compared to that seen in emission in T Tauri disks might be expected if the emission and absorption features probe the conditions at different disk heights. In their thermal-chemical models of irradiated disk atmospheres, Najita & Ádámkóvics (2017) find that NH_3 is abundant deeper in the atmosphere, and at lower gas temperature, than the region in which HCN and C_2H_2 are abundant. Thus, we expect a low $[\text{NH}_3/\text{HCN}]$ ratio in the HCN-emitting gas (Figure 17, blue line). Abundant but cool NH_3 located below the HCN-emitting gas would also produce weak to negligible emission (Figure 17, dashed red line).

In contrast, cool gas could still be readily detected in absorption in transitions out of the

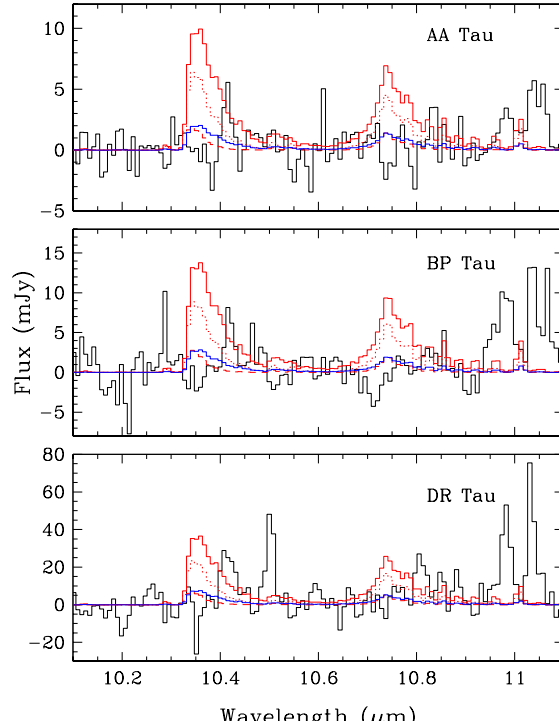


Fig. 17.— Observed spectra (black line) compared with simple slab emission models for NH_3 emission from inner T Tauri disks assuming $[\text{NH}_3/\text{HCN}]$ abundance ratios of 0.5 (red lines) and 0.1 (blue line) and HCN columns from Carr & Najita (2011) that assume optically thin emission, i.e., the HCN emission has the same emitting area as the water emission. Models at the higher abundance ratio are for temperatures of 600 K (solid red), 450 K (dotted red), and 300 K (dashed red); the model with the lower abundance ratio assumes 600 K. The three stars shown are ordered from low (AA Tau) to medium (BP Tau) to high (DR Tau) stellar accretion rate.

ground vibrational state, particularly with the large slant column densities for a disk viewed at high inclination. The cooler temperatures we measure for the NH_3 , HCN, and C_2H_2 absorption (450 K), compared to the typical temperatures of the HCN and C_2H_2 emission from T Tauri stars (600–1200 K; Carr & Najita 2011; Salyk et al. 2011) are consistent with the idea that the GV Tau N absorption probes a deeper layer in the disk atmosphere than the region responsible for the MIR molecular emission from T Tauri disks. The low temperatures we find for the NH_3 absorption (250 K in 2007 and 450 K in 2006) are roughly consistent with this explanation for the lack of detectable NH_3 emission from T Tauri disks and with the cooler temperatures anticipated for NH_3 compared to HCN from the disk thermal-chemical models.

The measured column densities of NH_3 and HCN in GV Tau N add to our current understanding of the nitrogen reservoir in disks. As described by Pontoppidan et al. (2019), nitrogen is highly depleted in the bulk Earth, by 5–6 orders of magnitude, compared to its cosmic abundance. The low abundance suggests that the bulk carrier of nitrogen in the material that formed the Earth was much more volatile than water, favoring a nitrogen-bearing molecule like N_2 , which has a low binding energy (430 K) compared to other potentially abundant molecules such as HCN and NH_3 .

(3610 K and 3130 K respectively; Walsh et al. 2015). Our results for GV Tau N are consistent with this picture. Because the measured column of NH_3 is modest, only comparable to that of HCN, it cannot be a major missing reservoir of nitrogen, and a molecule like N_2 is instead the likely dominant nitrogen reservoir.

5. Summary and Conclusions

The mid-infrared spectra of GV Tau N reported here were obtained with the original goal of studying the physical properties and molecular content of a disk viewed edge-on. The opportunity to study an unusually large column density of disk gas in absorption offered the potential to detect new molecular species. Consistent with that expectation, the TEXES spectra revealed the first evidence for NH_3 in the planet formation region of disks. The measured temperatures, molecular column densities, and column density ratios of the detected species (C_2H_2 , HCN, NH_3 , and H_2O) are consistent with the properties of a disk atmosphere within a few au of the star viewed at high inclination. While the NH_3 abundance measured here is higher than the upper limits obtained from molecular emission studies of disks, our results do confirm the expectation that NH_3 is not a major missing reservoir of nitrogen. If, as expected, the dominant nitrogen reservoir in inner disks is instead N_2 , its high volatility would make it difficult to incorporate into forming planets, a situation that may help to explain the low nitrogen content of the bulk Earth.

More interestingly, the TEXES spectra reveal an unexpected and significant redshift to the detected molecular absorption features, indicative of inflow at the disk surface. From the properties of the molecular absorption (column density, velocity shift), we can infer that the redshifted absorption carries a significant accretion rate: $\dot{M}_{\text{abs}} \sim 10^{-8} - 10^{-7} M_{\odot} \text{ yr}^{-1}$, comparable to the stellar accretion rates of active T Tauri stars. Thus we may be observing disk accretion in action. The results may provide observational evidence for a new disk accretion pathway for young protoplanetary disks: supersonic “surface accretion flows.” These flows have been found in MHD simulations of magnetized disks (e.g., Zhu & Stone 2018), but their potential role in young protoplanetary disks has received limited attention to date. The observed flows may also be related to accretion flows generated by magnetothermal winds. Future spectroscopy of the dynamics of other edge-on disks would help establish whether supersonic inward flows are common among young disks. In addition, future simulations are needed to understand whether supersonic surface accretion flows can be sustained under realistic ionization conditions in protoplanetary disks.

A. TEXES Spectra of GV Tau N

The figures in this section show the entire set of spectra of GV Tau N used in this study. Each panel shows the pipeline-reduced spectra on the observed wavelength scale before additional corrections were made to remove low-order structure in the continuum. Detected lines are annotated

at the velocity of the gaseous envelope surrounding GV Tau, $v_{\text{helio}} = 17.3 \text{ km s}^{-1}$ (or $v_{\text{LSR}} = 7.0 \text{ km s}^{-1}$; Hogerheijde et al. 1998). The molecular absorption features are clearly redshifted with respect to the envelope velocity.

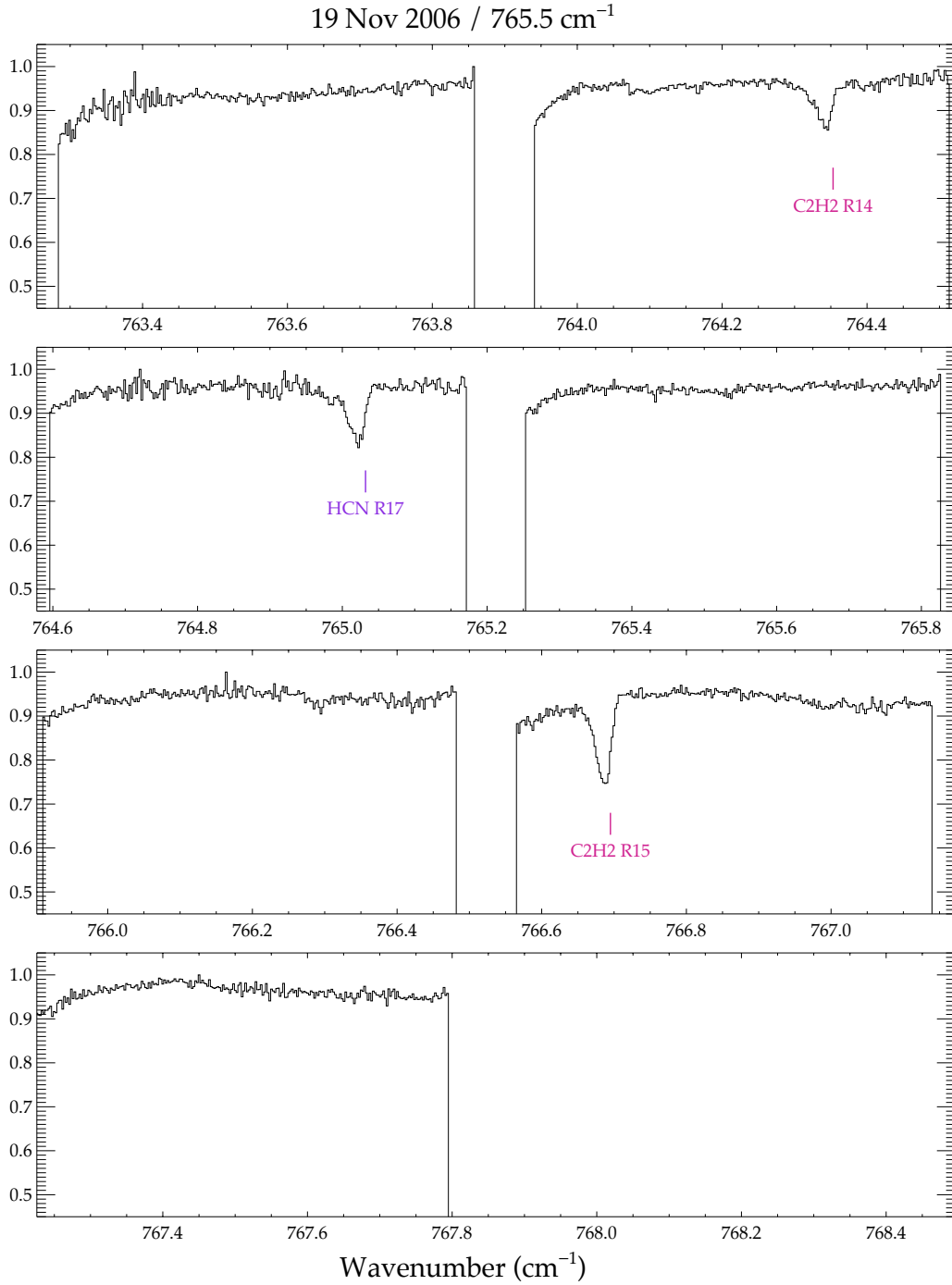


Fig. A1a.— TEXES pipeline-reduced spectra of GV Tau N, shown before additional corrections were made to remove low-order structure in the continuum. Absorption lines of C_2H_2 (red), HCN (purple), NH_3 (green), and water (blue) are marked in each panel, as is the $12 \mu\text{m}$ H_2 emission line (blue). This panel shows the GV Tau N spectrum observed in 2006 at the setting centered at 765.5 cm^{-1} .

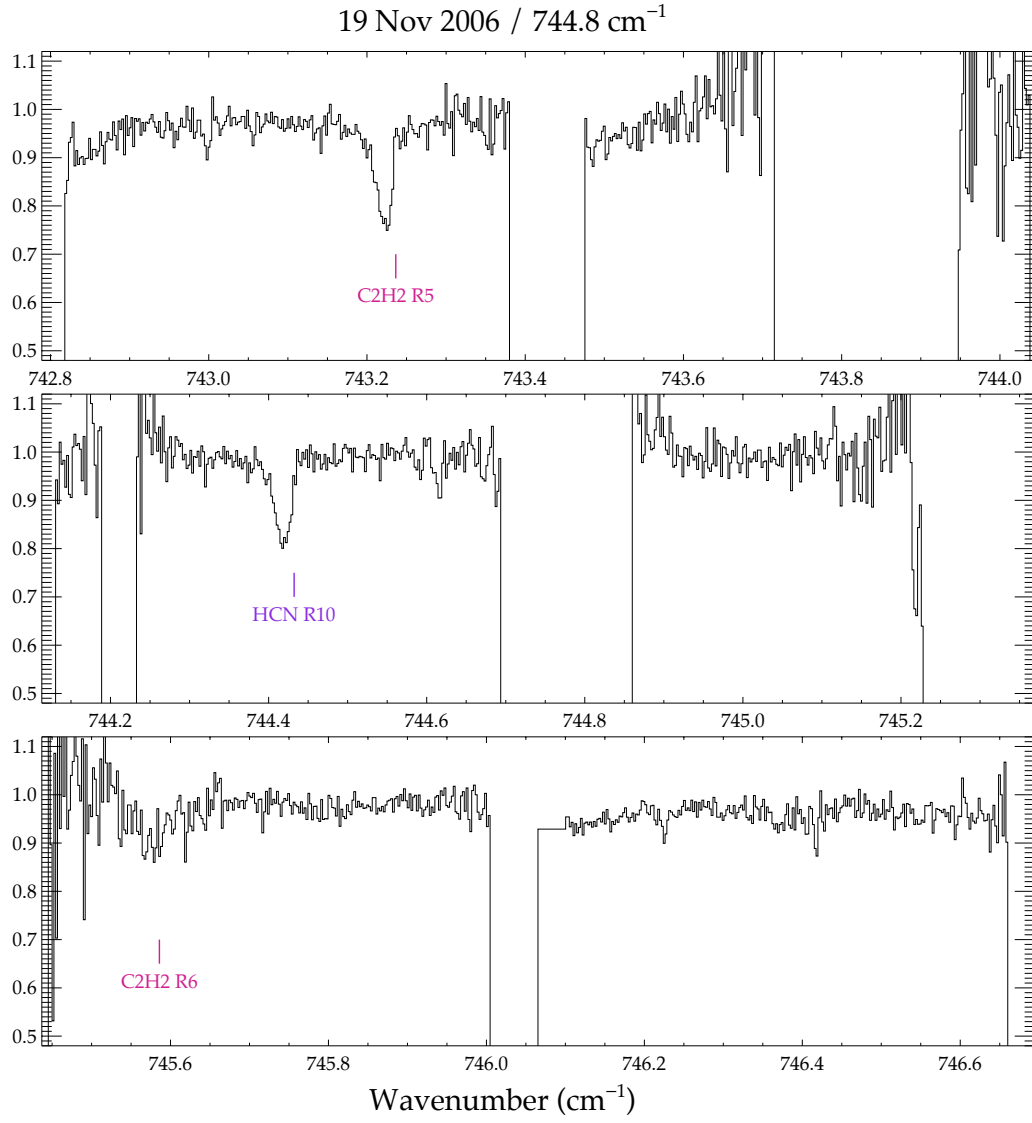


Fig. A1b.— As in Figure A1a, for the setting centered at 744.8 cm^{-1} observed in 2006.

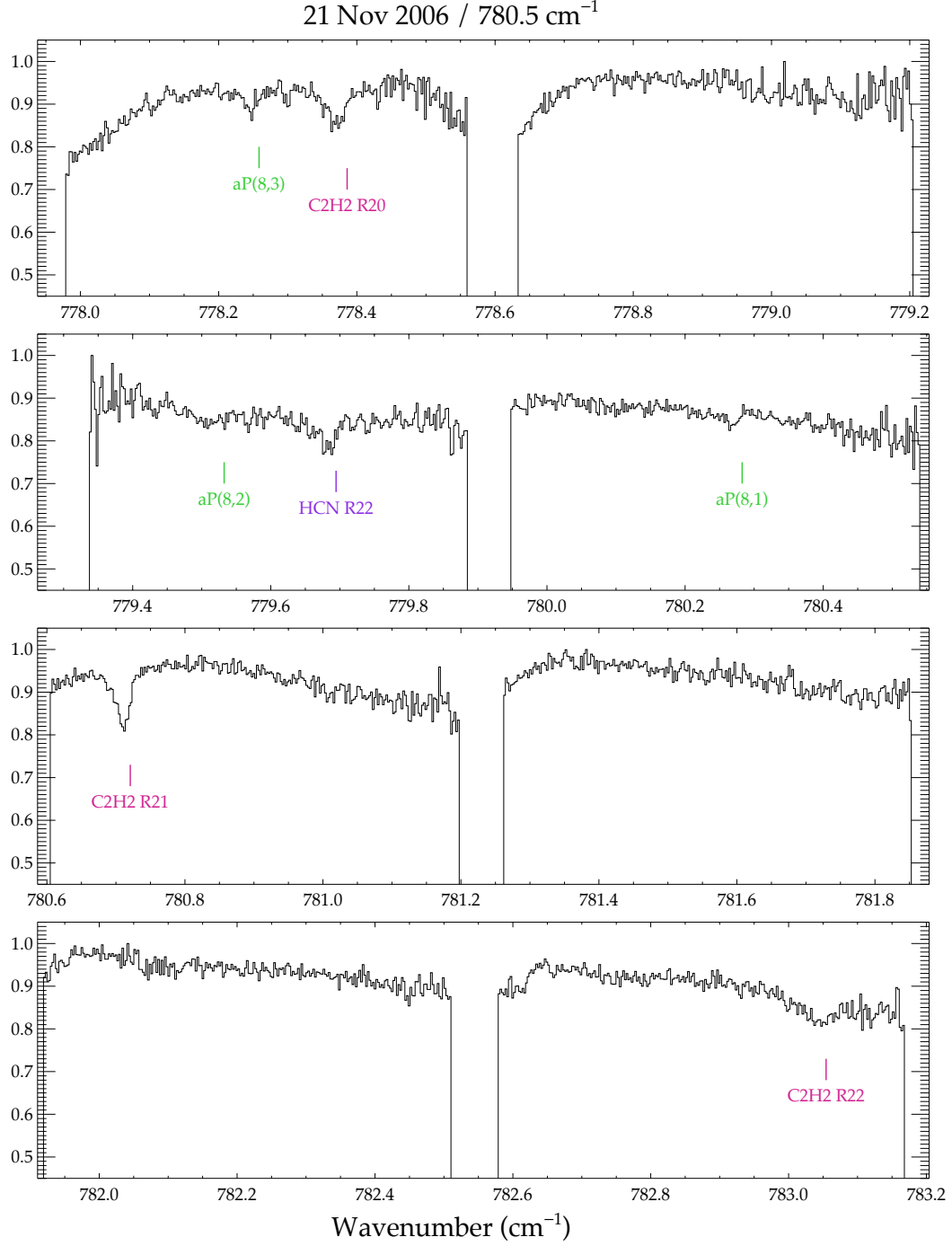


Fig. A1c.— As in Figure A1a, for the setting centered at 780.5 cm^{-1} observed in 2006.

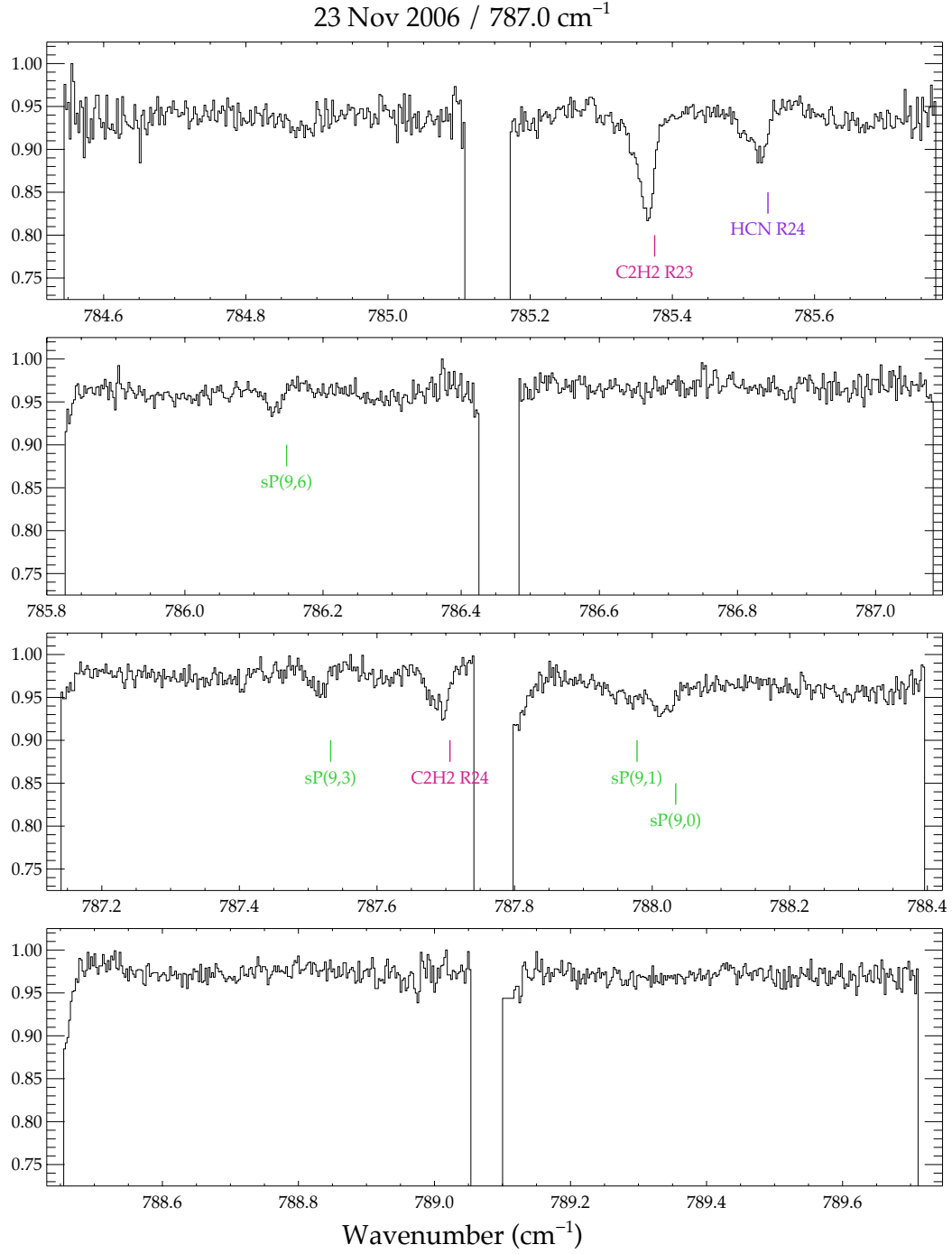


Fig. A1d.— As in Figure A1a, for the setting centered at 787.0 cm^{-1} observed in 2006.

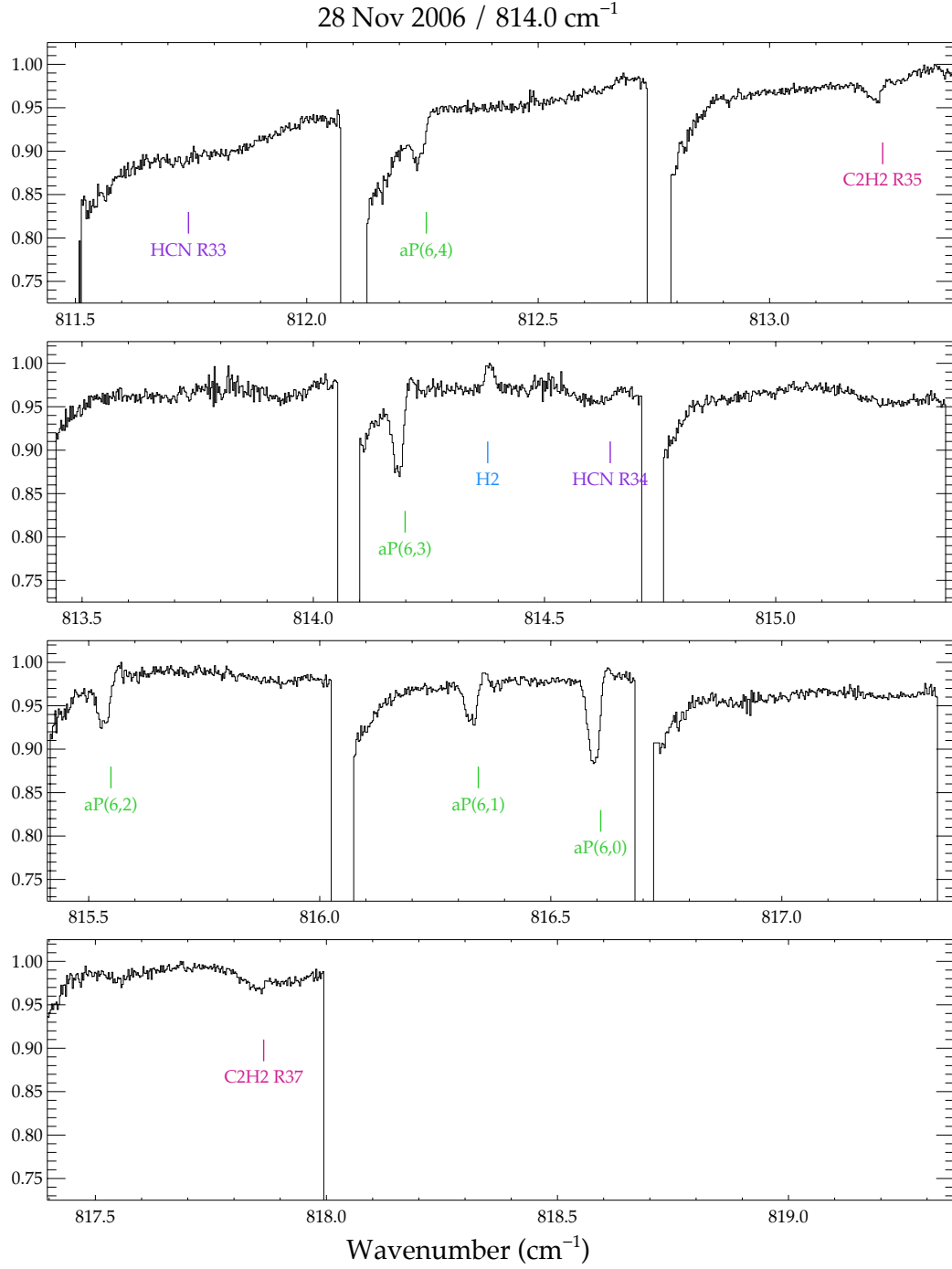


Fig. A1e.— As in Figure A1a, for the setting centered at 814.0 cm^{-1} observed in 2006.

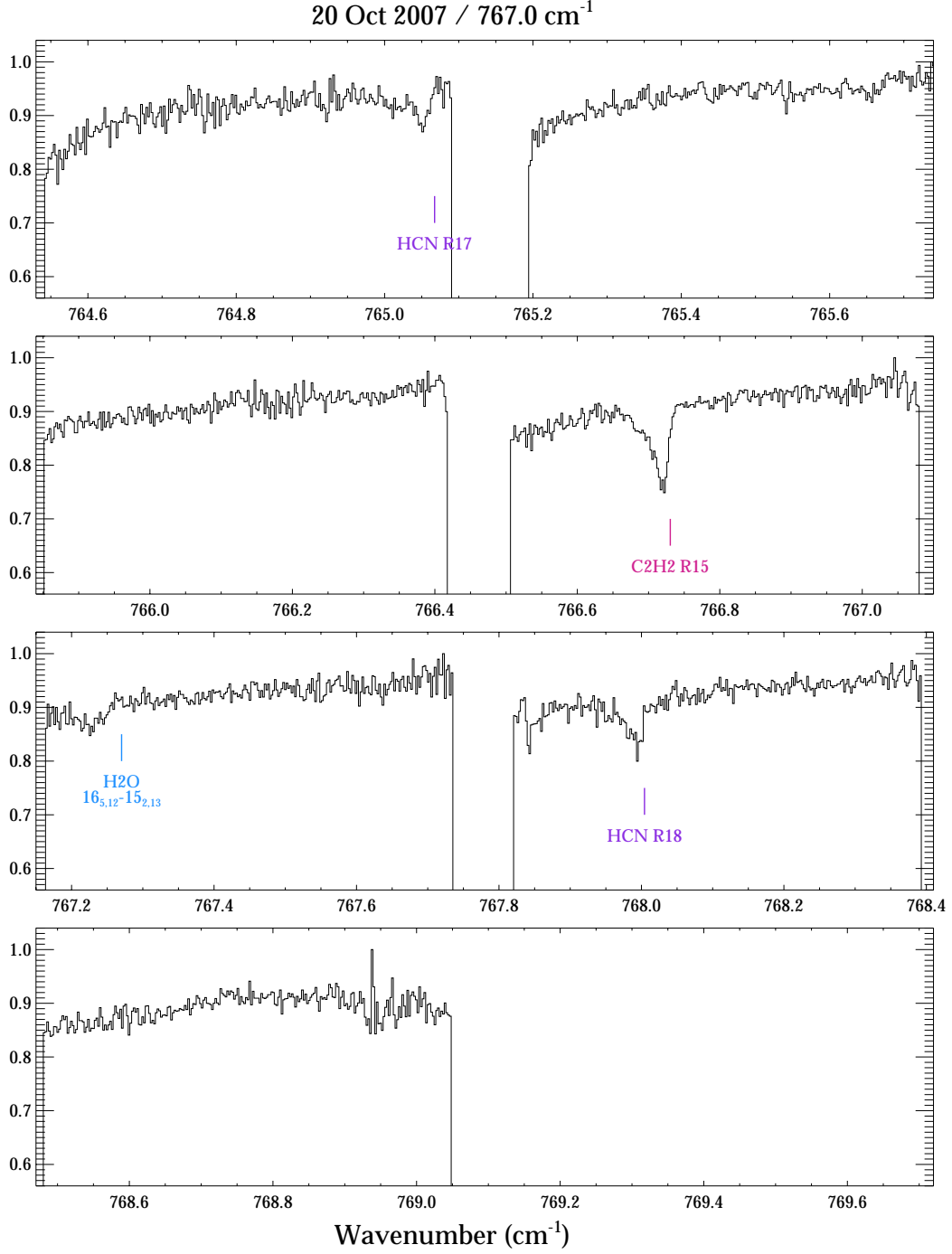


Fig. A1f.— As in Figure A1a, for the setting centered at 767.0 cm^{-1} observed in 2007.

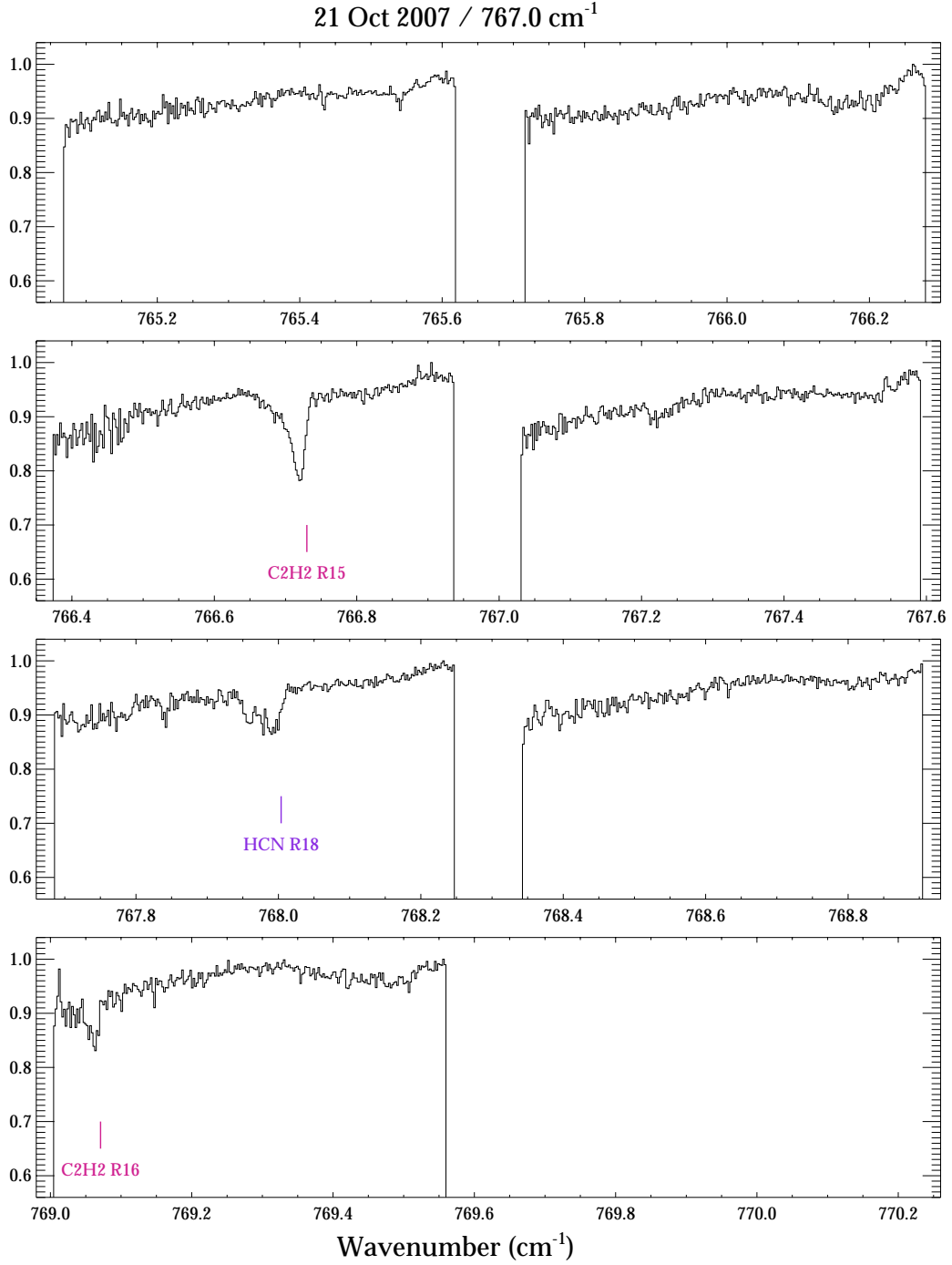


Fig. A1g.— As in Figure A1a, for the setting observed in 2007 centered one order to the red of the other setting at 767.0 cm⁻¹ shown in the previous panel.

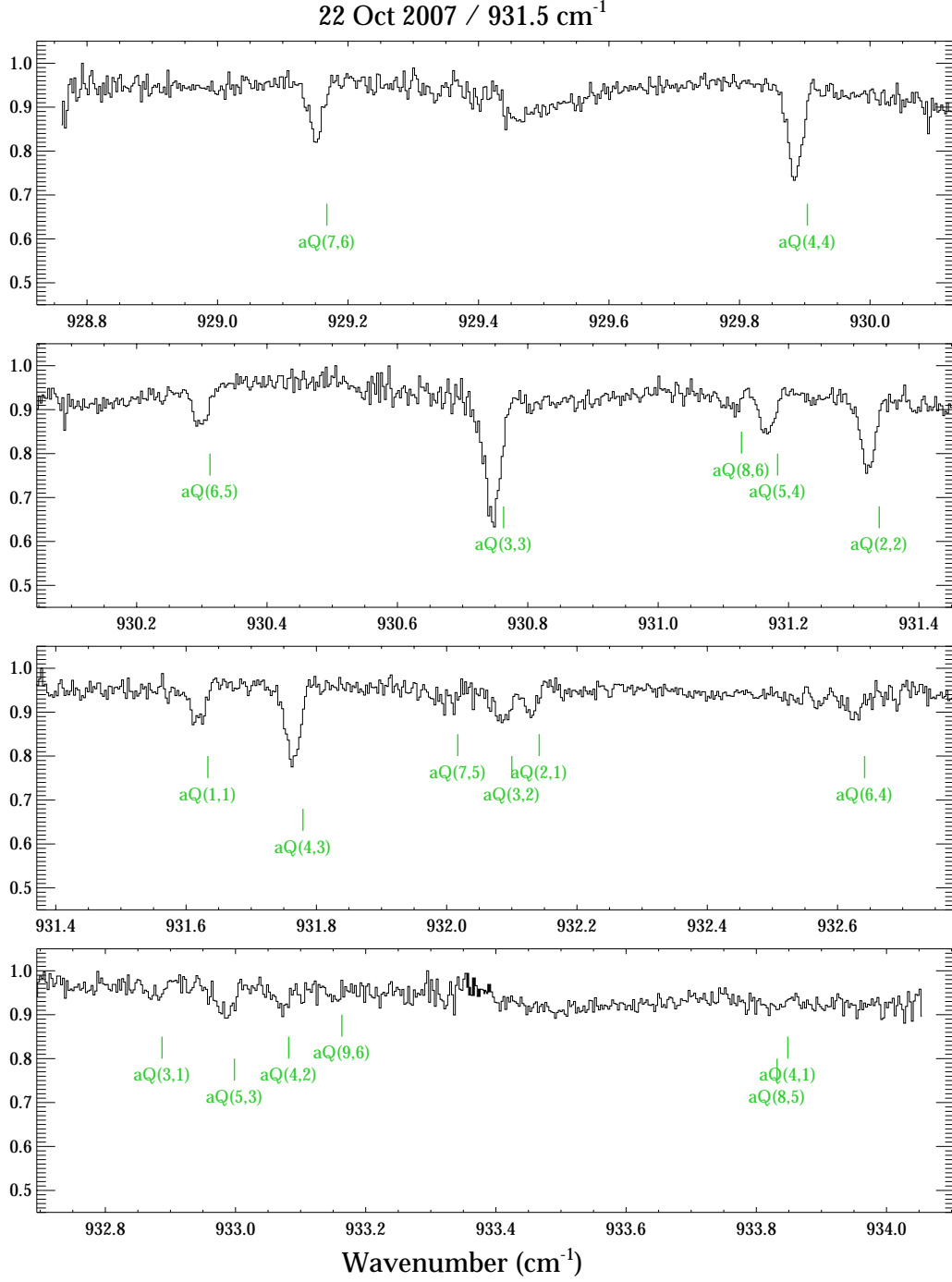


Fig. A1h.— As in Figure A1a, for the setting centered at 932.0 cm^{-1} observed in 2007.

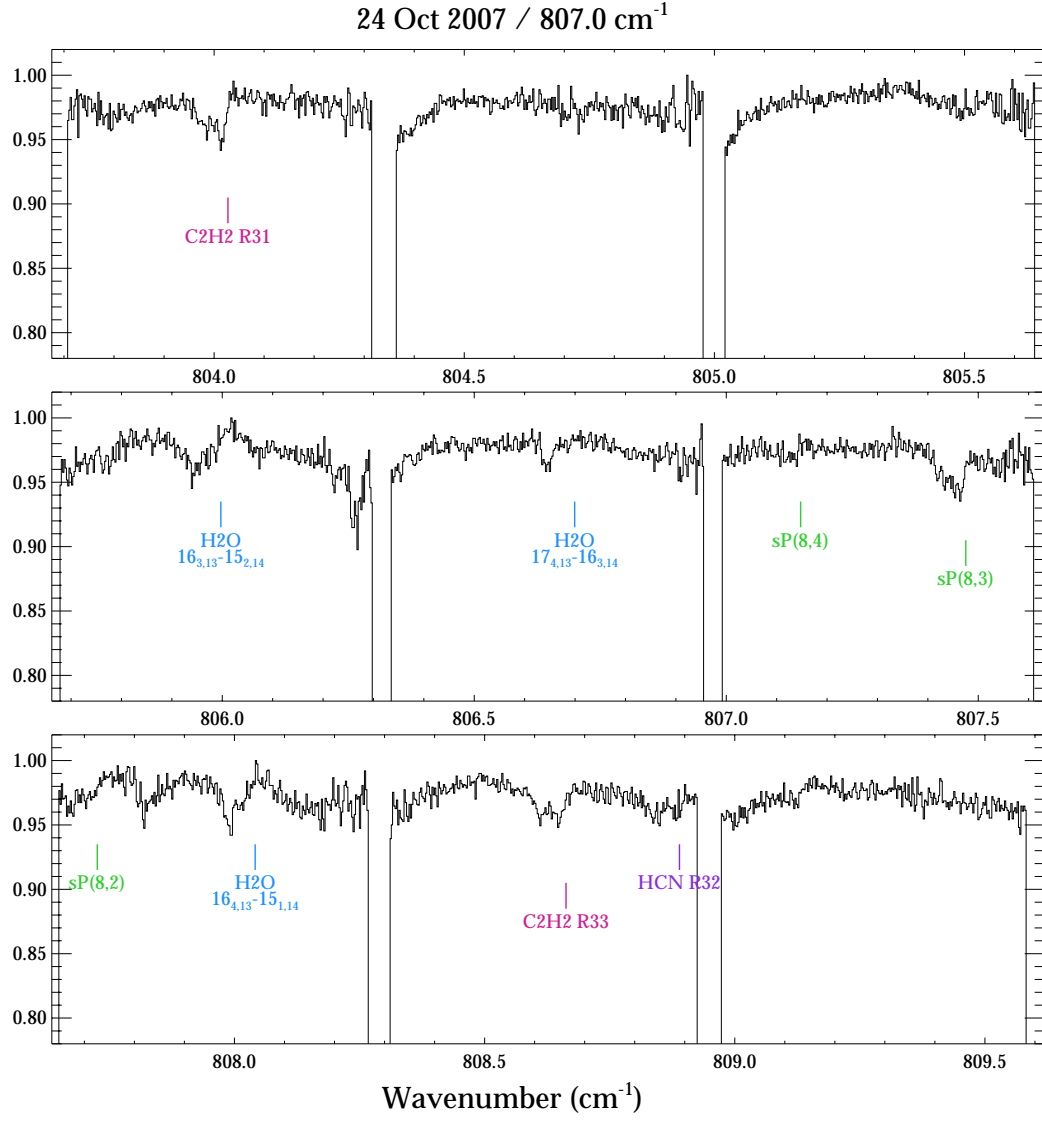


Fig. A1i.— As in Figure A1a, for the setting centered at 807.0 cm⁻¹ observed in 2007.

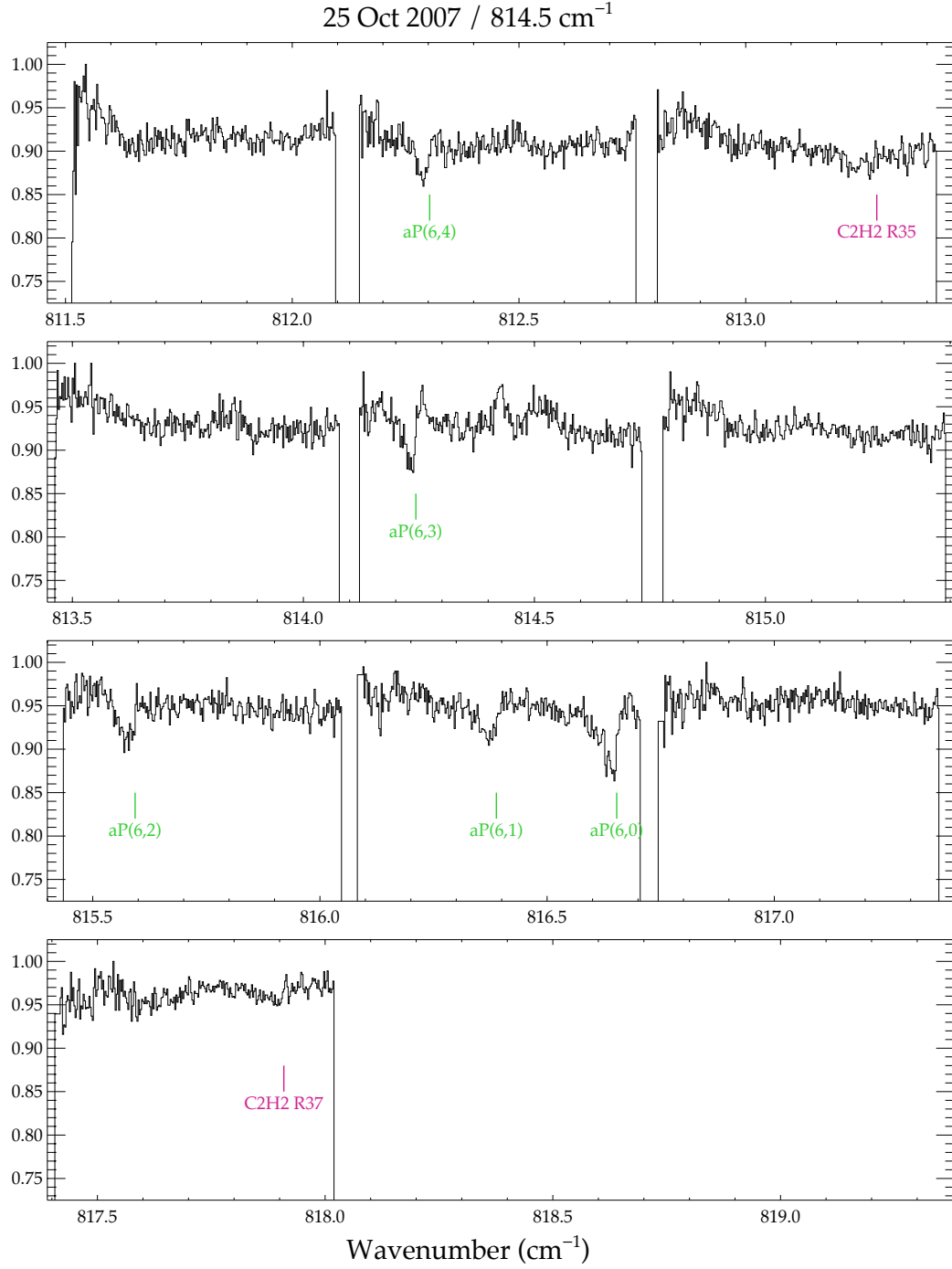


Fig. A1j.— As in Figure A1a, for the setting centered at 814.5 cm^{-1} observed in 2007.

We gratefully thank Zhaohuan Zhu for introducing us to his 2018 paper and for helpful discussion and advice. We also thank the referee for helpful comments that improved the manuscript. This work was performed in part at the Aspen Center for Physics which is supported by the National Science Foundation grant PHY-1607611. Work by SDB was performed in part at the National Optical Astronomy Observatory. NOAO is operated by the Association of Universities for Research in Astronomy (AURA), Inc. under a cooperative agreement with the National Science Foundation. SDB also acknowledges support from this work by NASA Agreement No. NXX15AD94G; NASA Agreement No. NNX16AJ81G; and NSF-AST 1517014.

The authors wish to recognize and acknowledge the very significant cultural role and reverence that the summit of Mauna Kea has always had within the indigenous Hawaiian community. We are most fortunate to have the opportunity to conduct observations from this mountain. We thank the Gemini staff, and John White in particular, for their support of TEXES observations on Gemini North. The development of TEXES was supported by grants from the NSF and the NASA/USRA SOFIA project. Modification of TEXES for use on Gemini was supported by Gemini Observatory. Observations with TEXES were supported by NSF grant AST 06-07312. M. J. R. acknowledges support from NSF grant AST 07-08074, NASA grant NNG04GG92G, and NASA Collaborative Agreement 80NSSC19K1701.

This work is based on observations obtained at the international Gemini Observatory, a program of NSF’s NOIRLab, which is managed by the Association of Universities for Research in Astronomy (AURA) under a cooperative agreement with the National Science Foundation on behalf of the Gemini Observatory partnership: the National Science Foundation (United States), National Research Council (Canada), Agencia Nacional de Investigación y Desarrollo (Chile), Ministerio de Ciencia, Tecnología e Innovación (Argentina), Ministério da Ciência, Tecnologia, Inovações e Comunicações (Brazil), and Korea Astronomy and Space Science Institute (Republic of Korea).

REFERENCES

- Bai, X. 2017, *ApJ*, 845, 75
- Bai, X. & Stone, J. M. 2013, *ApJ*, 769, 76
- Bast, J. E., Lahuis, F., van Dishoeck, E. F., & Tielens, A. G. G. M. 2013, *A&A*, 551, 118
- Beckwith, K., Hawley, J. F., & Krolík, J. H. 2009, *ApJ*, 707, 428
- Bender, C. 2010, in “Astronomy of Exoplanets with Precise Radial Velocities,” workshop at Penn State University, University Park, PA, <http://personal.psu.edu/jtw13/rvworkshop/>
- Bitner, M. A. et al. 2008, *ApJ*, 688, 1326
- Boogert, A. C. A., Hogerheijde, M. R., & Blake, G. A. 2002, *ApJ*, 568, 761
- Brittain, S. D., Rettig, T. W., Simon, T., Kulesa, C. 2005, *ApJ*, 626, 283
- Bruderer, S., Harsono, D., & van Dishoeck, E. F. 2015, *A&A*, 575, 94

- Carr, J. S., & Najita, J. R. 2008, *Science*, 319, 1504
- Carr, J. S., & Najita, J. R. 2011, *ApJ*, 733, 102
- Ceccarelli, C., Hollenbach, D. J., & Tielens, A. G. G. M. 1996, *ApJ*, 471, 400
- Davis, S., Teasley, T., Brittain, S. D., Doppmann, G., & Najita, J. R. 2015, *BAAS*, 225, 348.05
- Doppmann, G. W., Najita, J. R., & Carr, J. S. 2008, 685, 298
- Fuente, A., Treviño-Morales, S. P., Le Gal, R., Rivière-Marichalar, P., Pilleri, P., Rodríguez-Baras, M., & Navarro-Almaida, D. 2020, *MNRAS*, in press; arXiv:2006.15065
- Furlan, E., et al. 2008, *ApJS*, 176, 184
- Gammie, C. F. 1996, *ApJ*, 457, 355
- Gibb, E. L. & Horne, D. 2013, *ApJL*, 776, L28
- Gibb, E. L., Van Brunt, K. A., Brittain, S. D., & Rettig, T. W. 2007, *ApJ*, 660, 1572
- Guilet, J., & Ogilvie, G. I. 2012, *MNRAS*, 424, 2097
- Guilet, J., & Ogilvie, G. I. 2013, *MNRAS*, 430, 822
- Guilloteau, S., Dutrey, A., Piétu, V., & Boehler, Y. 2011, *A&A*, 529, 105
- Hartmann, L., Herczeg, G., & Calvet, N. 2016, *ARAA*, 54, 135
- Hogerheijde, M. R., van Dishoeck, E. F., Blake, G. A., & van Langevelde, H. J. 1998, *ApJ*, 502, 315
- Horne, D., Gibb, E., Rettig, T. W., Brittain, S., Tilley, D., & Balsara, D. 2012, *ApJ*, 754, 64
- Kruger, A. J., Richter, M. J., Carr, J. S., Najita, J. R., Doppmann, G., & Seifahrt, A., 2011, *ApJ*, 729, 145
- Lacy, J. H., Richter, M. J., Greathouse, T. K., Jaffe, D. T., & Zhu, Q. 2002, *PASP*, 114, 153
- Lahuis, F., van Dishoeck, E. F., Boogert, A. C. A., Pontoppidan, K. M., Blake, G. A., Dullemond, C. P., Evans, N. J., II, Hogerheijde, M. R., Jørgensen, J. K., Kessler-Silacci, J. E., Knez, C. 2006, *ApJ*, 636, L145
- Lee, S., Lee, J., Park, S., Lee, J.-J. Kidder, B., Mace, G. N., & Jaffe, D. T. 2016, *ApJ*, 826, 179
- Leinert, C., & Haas, M. 1989, *ApJ*, 342, L39
- Loomis, R. A., Öberg, K. I., Andrews, S. M., & MacGregor, A. 2017, *ApJ*, 840, 23
- Mandell, A. M., Bast, J., van Dishoeck, E. F., et al. 2012, *ApJ*, 747, 92
- Najita, J. R., Ádámkovics, M., & Glassgold, A. E. 2011, *ApJ*, 743, 147
- Najita, J. R., & Ádámkovics, M. 2017, *ApJ*, 847, 6
- Najita, J. R., & Bergin, E. A. 2018, *ApJ*, 864, 168
- Najita, J. R., Carr, J. S., Salyk, C., Lacy, J. H., Richter, M. J., & DeWitt, C. 2018, *ApJ*, 862, 122
- Pontoppidan, K. M., Blake, G. A., & Smette, A. 2011, *ApJ*, 733, 84

- Pontoppidan, K. M., Salyk, C., Banzatti, A., Blake, G. A., Walsh, C., Lacy, J. H., & Richter, M. J. 2019, *ApJ*, 874, 92
- Pontoppidan, K. M., et al. 2008, *ApJ*, 678, 1005
- Rettig, T., Brittain, S., Simon, T., Gibb, E., Balsara, D. S., Tilley, D. A., & Kulesa, C. 2006, 646, 342
- Roccatagliata, V., Ratzka, T., Henning, T., Wolf, S., Leinert, C., & Bouwman, J. 2011, *A&A*, 534, 33
- Rothman, L. S., Gordon, I. E., Babikov, Y., et al. 2013, *JQSRT*, 130, 4
- Fischer, J., Gamache, R. R., Goldman, A., Rothman, L. S., & Perrin, A. 2003, *JQSRT*, 82, 401
- Salinas, V. N. et al. 2016, *A&A*, 591, 122
- Salyk, C., Pontoppidan, K. M., Blake, G. A., Najita, J. R., & Carr, J. S. 2011, *ApJ*, 731, 130
- Sheehan, P. D., & Eisner, J. A. 2014, *ApJ*, 791, 19
- Simon, M., Dutrey, A., Guilloteau, S. 2000, *ApJ*, 545, 1034
- Smith, R. L., Pontoppidan, K. M., Young, E. D., & Morris, M. R. 2015, *ApJ*, 813, 120
- Stone, J. M., & Norman, M. L. 1994, *ApJ*, 433, 746
- Turner, N. J., Fromang, S., Gammie, C., Klahr, H., Lesur, G., Wardle, M., Bai, X.-N. 2014, in “Protostars and Planets VI”, eds. H. Beuther, R. S. Klessen, C. P. Dullemond, & T. Henning, (Tucson: University of Arizona Press), p. 411-432
- Walsh, C., Nomura, H., & van Dishoeck, E. 2015, *A&A*, 582, 88
- Walsh, C., Daley, C., Facchini, S., & Juhász 2017, *A&A* 607, 114
- Woitke, P. et al. 2018, *A&A*, 618, 57
- Zhang, K., Crockett, N., Salyk, C., Pontoppidan, K., Turner, N., J., Carpenter, J. M., & Blake, G., A. 2015, *ApJ*, 805, 55
- Zhu, Z. & Stone, J. M. 2018, *ApJ*, 857, 34

Table 1. Observations

UT Date	Central Waveno. (cm^{-1})	Clock Time (minutes)	Calibrator
Nov 19, 2006	765.5	57	Sirius
Nov 19, 2006	744.8	55	Sirius
Nov 21, 2006	780.5	42	Sirius
Nov 23, 2006	787.0	87	BN ^a
Nov 28, 2006	814.0	55	BN
Oct 20, 2007	767.0	63	Ceres
Oct 21, 2007	767.0	57	Ceres
Oct 22, 2007	931.5	145	Sirius
Oct 24, 2007	807.0	114	Flora
Oct 25, 2007	814.5	56	Flora

^aWe have not found narrow spectral features towards BN in any previous TEXES observing.

Table 2. All Lines

Line	E_ℓ (cm ⁻¹)	wave (cm ⁻¹)	g_ℓ	A (s ⁻¹)	2006 [†]	2007 [†]
C ₂ H ₂						
R5	35.3	743.26389	33	3.441	*	-
R6	49.4	745.61349	13	3.439	* _c	-
R14	247	764.38213	29	3.586	*	-
R15	282.3	766.72409	93	3.615	*	*
R16	319.9	769.065	33	3.646	-	* _b
R20	493.9	778.4173	41	3.782	*	-
R21	543.3	780.75233	129	3.82	*	-
R22	595	783.08606	45	3.858	*	-
R23	649	785.41845	141	3.897	*	-
R24	705.4	787.74946	49	3.939	* _b	-
R31	1165.6	804.0242	189	4.259	-	*
R33	1318.2	808.65925	201	4.362	-	*
R35	1480	813.28707	213	4.47	*	*
R37	1651.2	817.90731	225	4.583	*	*
R14 [‡]	859.5	766.3327	87	2.201	*	-
HCN						
R10	162.6	744.459871	126	1.221	*	-
R17	452.1	765.061068	210	1.302	*	*
R18	505.2	767.997835	222	1.315	-	*
R22	747.2	779.726066	270	1.365	*	-
R24	885.9	785.577741	294	1.391	*	-
R32	1557.8	808.885973	390	1.491	-	*
R33	1654.9	811.787019	402	1.504	*	x
R34	1755	814.685003	414	1.516	*	x
NH ₃ 780 cm-1						
aP(8,3)	679.84	778.289947	204	4.034	*	-
aP(8,2)	697.92	779.56397	102	4.396	*	-
aP(8,1)	708.75	780.314123	102	4.611	*	-

Table 2—Continued

Line	E_ℓ (cm ⁻¹)	wave (cm ⁻¹)	g_ℓ	A (s ⁻¹)	2006 [†]	2007 [†]
NH ₃ 787 cm-1						
sP(9,8)	655.65	784.980474	102	0.985	x	-
sP(9,7)	710.86	785.596321	102	1.835	xd	-
sP(9,6)	758.39	786.190618	204	2.559	*	-
sP(9,5)	798.37	786.732259	102	3.161	xa	-
sP(9,3)	856.18	787.576089	204	4.022	*	-
sP(9,1)	884.92	788.021449	102	4.448	*c	-
sP(9,0)	888.5	788.077694	204	4.499	*	-
NH ₃ 807 cm-1						
sP(8,7)	532.89	805.778993	102	1.185	-	x
sP(8,6)	580.78	806.274244	204	2.191	-	xa
sP(8,5)	621.07	806.737711	102	3.029	-	x
sP(8,4)	653.87	807.144082	102	3.705	-	*
sP(8,3)	679.29	807.471806	204	4.221	-	*
sP(8,2)	697.4	807.722297	102	4.596	-	*
sP(8,1)	708.24	807.871595	102	4.814	-	xa
NH ₃ 814 cm-1						
aP(6,4)	358.28	812.301065	66	3.093	*	*
aP(6,3)	383.98	814.241452	132	4.165	*	*
aP(6,2)	402.28	815.591036	66	4.927	*	*
aP(6,1)	413.24	816.386201	66	5.383	*	*
aP(6,0)	416.89	816.650974	132	5.53	*	*
NH ₃ 931 cm-1						
aQ(7,6)	423.22	929.161734	180	9.809	-	*
aQ(4,4)	140.16	929.898105	54	12.18	-	*
aQ(9,7)	711.55	929.970478	114	8.306	-	x
aQ(6,5)	325.13	930.306609	78	9.058	-	*
aQ(3,3)	86.66	930.757026	84	11.39	-	*
aQ(11,8)	1070.38	931.062178	138	7.391	-	x

Table 2—Continued

Line	E_ℓ (cm ⁻¹)	wave (cm ⁻¹)	g_ℓ	A (s ⁻¹)	2006 [†]	2007 [†]
aQ(8,6)	1581.47	931.122022	204	7.607	-	*
aQ(5,4)	239.41	931.177341	66	8.098	-	*
aQ(2,2)	45.59	931.333247	30	10.11	-	*
aQ(1,1)	17	931.6277	18	7.583	-	*
aQ(4,3)	166.09	931.773553	108	6.823	-	*
aQ(7,5)	463.71	932.011207	90	6.775	-	*
aQ(3,2)	105.18	932.094036	42	5.049	-	*
aQ(2,1)	56.71	932.136158	30	2.524	-	*
aQ(6,4)	358.28	932.635696	78	5.77	-	*
aQ(3,1)	116.28	932.881207	42	1.26	-	*
aQ(5,3)	265.23	932.9923	132	4.539	-	*
aQ(4,2)	184.55	933.075823	54	3.025	-	*
aQ(9,6)	759	933.157383	228	6.063	-	*
aQ(8,5)	621.69	933.82604	102	5.251	-	*d
aQ(4,1)	195.61	933.84251	54	0.755	-	*d
H ₂ O						
16 _{5,12} –15 _{2,13}	2872.3	767.263798	93	6.761	-	*
16 _{3,13} –15 _{2,14}	2631.3	805.99363	31	4.217	-	*
17 _{4,13} –16 _{3,14}	3211.2	806.69564	99	7.665	-	*
16 _{4,13} –15 _{1,14}	2631.3	808.03788	93	4.211	-	*
7 _{6,1} –6 _{1,6}	447.25	768.9422	39	2.6×10^{-4}	-	x
8 _{7,2} –7 _{2,5}	782.41	808.2803	45	1.2×10^{-3}	-	x
9 _{9,0} –8 _{6,3}	1411.61	813.8577	68 ^e	0.021	-	x
14 _{9,6} –13 _{6,7}	2756.41	928.9932	81	0.767	-	x

[†]* (detection); x (non-detection); - (not covered); a (telluric line); b (order edge/roll-off); c (high uncertainty); d (blended with other line).

[‡] $\nu_4+\nu_5-\nu_4$ band; i.e., absorption out of the ν_4 level.

^eThe 813.85 cm⁻¹ ortho and 813.83 cm⁻¹ para H₂O lines were treated as a single line with combined g_ℓ .

Table 3. Line EWs from 2006

ID	Wave (cm ⁻¹)	S/N [†]	EW(LV) (cm ⁻¹)	err	EW(HV) (cm ⁻¹)	err	EW (cm ⁻¹)	err	Dep(LV)	Dep(HV)
C₂H₂										
R5	743.2639	60	4.373	0.232	1.502	0.245	5.874	0.428	0.134	0.043
R14	764.3821	135	2.100	0.100	0.869	0.106	2.969	0.183	0.063	0.024
R15	766.7241	135	4.184	0.098	1.189	0.104	5.373	0.178	0.125	0.033
R20	778.4173	80	1.478	0.177	0.630	0.198	2.108	0.337	0.046	0.017
R21	780.7523	78	2.879	0.149	0.652	0.156	3.531	0.252	0.083	0.018
R22	783.0861	90	1.238	0.163	0.524	0.163	1.761	0.292	0.036	0.015
R23	785.4185	95	2.750	0.132	0.949	0.138	3.699	0.231	0.080	0.026
R24	787.7495	100	1.010	0.108	0.458	0.113	1.468	0.177	0.029	0.012
R35	813.2870	430	0.456	0.059	0.249	0.038	0.706	0.070	0.013	0.006
R37	817.9073	330	0.218	0.033	0.206	0.034	0.424	0.053	0.006	0.006
R14 [‡]	766.3327	100	0.569	0.089	[0.153	0.093]	0.722	0.129	0.017	0.004
HCN										
R10	744.4599	60	3.419	0.163	1.131	0.179	4.550	0.273	0.112	0.032
R17	765.0611	100	2.660	0.124	1.153	0.131	3.813	0.220	0.080	0.032
R22	779.7261	95	1.591	0.145	0.851	0.162	2.442	0.274	0.049	0.023
R24	785.5778	95	1.286	0.109	0.780	0.114	2.066	0.174	0.037	0.021
R33	811.7870	250	0.150	0.041	0.118	0.043	0.267	0.064	0.004	0.003
R34	814.6850	280	0.150	0.040	0.102	0.042	0.252	0.066	0.004	0.003
NH₃										
aP(8,3)	778.2899	120	0.808	0.072	[0.150	0.062]	0.958	0.095	0.027	0.007
aP(8,2)	779.5640	85	0.575	0.101	0.244	0.088	0.819	0.134	0.019	0.011
aP(8,1)	780.3141	135	0.431	0.061	0.202	0.058	0.633	0.084	0.016	0.008
sP(9,6)	786.1906	150	0.519	0.057	0.296	0.052	0.815	0.077	0.018	0.012
sP(9,3)	787.5761	100	0.438	0.082	0.330	0.078	0.768	0.113	0.016	0.013
sP(9,0)	788.0777	130	0.726	0.066	0.478	0.057	1.205	0.087	0.025	0.022
aP(6,4)	812.3011	180	0.801	0.048	0.332	0.044	1.133	0.065	0.027	0.013
aP(6,3)	814.2415	165	1.868	0.052	0.636	0.048	2.504	0.071	0.062	0.025
aP(6,2)	815.5911	250	0.932	0.035	0.332	0.032	1.264	0.047	0.031	0.013
aP(6,1)	816.3862	290	0.949	0.030	0.309	0.027	1.259	0.040	0.032	0.012
aP(6,0)	816.6510	350	2.195	0.025	0.680	0.023	2.875	0.033	0.073	0.027

Note. — [†] Continuum signal-to-noise per pixel; [‡] $\nu_4 + \nu_5 - \nu_4$ band (i.e., absorption out of the ν_4 level); LV indicates the low velocity component ($< 26 \text{ km s}^{-1}$) and HV the high velocity component ($> 26 \text{ km s}^{-1}$); EW is the sum of the contributions from the LV and HV components; err, the uncertainty on the EW, includes both the pixel-to-pixel noise and an estimate of the uncertainty in the continuum placement.

Table 4. Line EWs from 2007

ID	Wave cm ⁻¹	S/N [†]	EW(LV) cm ⁻¹	err	EW(HV) cm ⁻¹	err	EW cm ⁻¹	err	Dep(LV)	Dep(HV)
C₂H₂										
R15	766.7241	180	2.946	0.059	2.053	0.093	5.000	0.134	0.115	0.044
R16	769.0650	65	1.452	0.126	1.351	0.177	2.804	0.232	0.057	0.029
R31	804.0242	200	0.603	0.043	0.837	0.065	1.440	0.085	0.024	0.017
R33	808.6592	200	0.420	0.050	0.814	0.073	1.235	0.103	0.015	0.017
R35	813.2870	90	0.243	0.094	0.541	0.127	0.784	0.158	0.009	0.011
R37	817.9073	100	0.228	0.100	0.214	0.130	0.442	0.164	0.009	0.004
HCN										
R17	765.0611	60	1.222	0.253	1.358	0.584	2.580	0.603	0.051	0.029
R18	767.9979	150	1.413	0.124	1.108	0.190	2.522	0.267	0.055	0.024
R32	808.8860	200	0.252	0.055	0.501	0.089	0.754	0.097	0.009	0.010
NH₃										
sP(8,4)	807.1441	200	0.186	0.049	0.349	0.062	0.535	0.090	0.007	0.009
sP(8,3)	807.4718	180	0.474	0.052	0.627	0.061	1.102	0.084	0.016	0.016
sP(8,2)	807.7223	180	0.207	0.055	0.459	0.071	0.666	0.103	0.007	0.011
aP(6,4)	812.3011	100	0.975	0.192	0.482	0.249	1.456	0.421	0.033	0.012
aP(6,3)	814.2415	100	1.569	0.185	1.198	0.239	2.767	0.403	0.052	0.030
aP(6,2)	815.5911	90	0.911	0.149	0.903	0.188	1.814	0.302	0.030	0.022
aP(6,1)	816.3862	80	0.983	0.118	0.810	0.140	1.794	0.197	0.032	0.020
aP(6,0)	816.6510	95	1.683	0.101	1.077	0.120	2.760	0.170	0.055	0.027
aQ(7,6)	929.1617	75	2.709	0.148	0.602	0.093	3.311	0.188	0.085	0.041
aQ(4,4)	929.8981	100	3.980	0.120	1.538	0.076	5.518	0.161	0.136	0.105
aQ(6,5)	930.3066	90	1.975	0.113	0.265	0.074	2.240	0.139	0.062	0.018
aQ(3,3)	930.7570	40	5.858	0.287	1.764	0.178	7.622	0.368	0.181	0.120
aQ(8,6)	931.1220	90	1.092	0.124	0.398	0.078	1.490	0.157	0.034	0.027
aQ(5,4)	931.1774	90	2.318	0.116	0.534	0.075	2.852	0.144	0.072	0.037
aQ(2,2)	931.3333	80	3.303	0.142	1.215	0.102	4.517	0.198	0.113	0.069
aQ(1,1)	931.6277	80	1.851	0.129	0.416	0.087	2.267	0.166	0.063	0.029
aQ(4,3)	931.7736	80	3.757	0.138	1.067	0.100	4.825	0.189	0.128	0.061
aQ(7,5)	932.0112	80	0.712	0.147	0.293	0.090	1.006	0.191	0.022	0.020
aQ(3,2)	932.0941	85	2.141	0.155	0.488	0.091	2.629	0.206	0.067	0.033
aQ(2,1)	932.1362	85	1.309	0.149	0.341	0.088	1.651	0.195	0.041	0.023
aQ(6,4)	932.6357	65	0.936	0.161	0.175	0.105	1.112	0.201	0.029	0.012
aQ(3,1)	932.8812	70	0.812	0.135	[0.057	0.104	0.869	0.174	0.028	0.003
aQ(5,3)	932.9923	70	1.678	0.136	0.565	0.104	2.242	0.175	0.057	0.032
aQ(4,2)	933.0758	70	0.967	0.147	0.210	0.096	1.177	0.182	0.030	0.014
aQ(9,6)	933.1574	70	0.381	0.148	[-0.01	0.096	0.365	0.183	0.012	-0.001
H₂O										
16 _{5,12} –15 _{2,13}	767.2638	150	0.055	0.044	0.967	0.118	1.022	0.130	0.003	0.022
16 _{3,13} –15 _{2,14}	805.9937	160	0.217	0.047	0.815	0.132	1.032	0.140	0.012	0.018
17 _{4,13} –16 _{3,14}	806.6956	215	0.078	0.037	0.546	0.071	0.624	0.080	0.004	0.012
16 _{4,13} –15 _{1,14}	808.0379	160	0.214	0.055	0.935	0.082	1.149	0.099	0.011	0.021

Table 4—Continued

ID	Wave cm ⁻¹	S/N [†]	EW(LV) cm ⁻¹	err	EW(HV) cm ⁻¹	err	EW cm ⁻¹	err	Dep(LV)	Dep(HV)
7 _{6,1} –6 _{1,6}	768.9422	63	-	-	<0.52	-	<0.52	-	-	-
8 _{7,2} –7 _{2,5}	808.2803	85	-	-	<0.39	-	<0.39	-	-	-
9 _{9,0} –8 _{6,3}	813.8577	85	-	-	<0.45	-	<0.45	-	-	-
14 _{9,6} –13 _{6,7}	928.9932	110	-	-	<0.51	-	<0.51	-	-	-

Note. — [†] Continuum signal-to-noise per pixel; LV indicates the low velocity component ($< 26 \text{ km s}^{-1}$) and HV the high velocity component ($> 26 \text{ km s}^{-1}$); EW is the sum of the contributions from the LV and HV components; err, the uncertainty on the EW, includes both the pixel-to-pixel noise and an estimate of the uncertainty in the continuum placement; upper limits are $2\text{-}\sigma$.

Table 5. COG Results 2006

Molecule	Comp	No.*	T (K)	σ	$N/\Delta v$ (10^{16} cm^{-2} / km s^{-1})	σ	$f \Delta v$ (km s^{-1})	σ	$f N$ (10^{16} cm^{-2})	σ	χ_r^2	τ_{max}	N^\dagger (10^{17} cm^{-2})
C ₂ H ₂	LV	11	445	$^{+20}_{-20}$	1.66	$^{+0.38}_{-0.34}$	1.37	$^{+0.25}_{-0.16}$	2.27	$^{+0.18}_{-0.16}$	1.46	2.1 (R15)	3.3
	HV	10	485	$^{+65}_{-75}$	5.5	$^{+6.0}_{-2.3}$	0.27	$^{+0.10}_{-0.08}$	1.46	$^{+0.86}_{-0.30}$	1.3	6.0 (R15)	11
HCN	LV	6	465	$^{+100}_{-65}$	3.55	$^{+4.6}_{-3.1a}$	1.24	$^{+6.76a}_{-0.46}$	4.40	$^{+1.94}_{-1.08}$	0.32	1.77 (R10)	7.1
	HV	6	410	$^{+230}_b$	23.4	$^{+0.83}_b$	0.23	$^{+0.83}_b$	5.37	$^{+0.11}_{-0.06}$	0.15	13.6 (R10)	46.8
NH ₃	LV	11	455	$^{+45}_{-40}$	0.2-0.7	c	2.6-8.0	c	1.79	$^{+2.50}_{-0.62}$	1.74	0.09-0.3	0.4-1.4
	HV	11	880	$^{+380}_{-230}$	3.31	$^{+8.2}_{-3.2d}$	0.51	$^{+7.50d}_{-0.29}$	1.69		1.41	0.56 (aP(6,0))	6.6

*Number of lines used in the fit.

[†]Assumes $\Delta v = 2 \text{ km s}^{-1}$.

^aLower bound on $N/\Delta v$ set by upper bound $f_d \Delta v = 8.0 \text{ km s}^{-1}$.

^bNo upper bound on $N/\Delta v$ or $f_d N$; no lower bound on T or $f_d \Delta v$.

^cBest fits are optically thin; hence T and $f_d N$ are well constrained, but not $f_d \Delta v$ and $N/\Delta v$; upper limit imposed on $f_d \Delta v = 8.0 \text{ km s}^{-1}$, which is also the minimum χ^2 ; hence range given for $N/\Delta v$, $f_d \Delta v$ and τ (and f_d).

^dImposing bound on $f_d \Delta v = 8.0 \text{ km s}^{-1}$ gives a lower bound on $N/\Delta v$ (optically thin).

Table 6. COG Results 2007

Molecule	Comp	No.*	T (K)	σ	$N/\Delta v$ (10^{16} cm^{-2} / km s^{-1})	σ	$f \Delta v$ (km s^{-1})	σ	$f N$ (10^{16} cm^{-2})	σ	χ_r^2	τ_{max}	N^\dagger (10^{16} cm^{-2})
C_2H_2	LV	6	435	+40 -40	1.9	+0.98 -0.76	0.88	+0.37 -0.17	1.67	+0.3 -0.24	0.25	2.47 (R15)	3.8
	HV	6	520	+100 -115	5.75	+6.3 -2.2	0.46	+0.18 -0.10	2.64	+1.6 -0.29	1.6	5.55 (R15)	11.5
HCN	LV	3	435 ^a		3	+1.4 -1.1	0.88 ^a		2.65	+0.4 -0.31	8.94	1.0 (R17)	6
	HV	3	520 ^a		13.5	+30 -6.6	0.46 ^a		6.18	+9.4 -2.10	5.2	4.1 (R17)	27
NH_3	LV	25	250	+10 -10	1.41	+0.29 -0.32	1.29	+0.28 -0.16	1.82	+0.1 -0.11	1.58	2.9 (aQ(3,3))	2.8
	HV	8 ^b	335	+200 -180	8.91	+173 -6.2	0.25	+0.29 -0.10	2.27	+26. -0.81	0.53	4.1 (aP(6,0))	17.8
H_2O	HV	8	450	+140 -65	2900	+9.7 -2.1	0.21	+0.08 -0.05	610.	+18. -5.0	1.10	5.3 (16,4,13-15,1,14)	5800

*Number of lines used in the fit.

[†] Assumes $\Delta v = 2 \text{ km s}^{-1}$.

^a Assumes temperatures and $f \Delta v$ from fit to C_2H_2 .

^b Only P-branch lines used in fit.